

# Ionised gas abundances in barred spiral galaxies<sup>★,★★</sup>

E. Florido<sup>1,2</sup>, I. Pérez<sup>1,2</sup>, A. Zurita<sup>1,2</sup>, and P. Sánchez-Blázquez<sup>3</sup>

<sup>1</sup> Dpto. de Física Teórica y del Cosmos, University of Granada, Facultad de Ciencias (Edificio Mecenas), 18071 Granada, Spain  
e-mail: [estrella;isa]@ugr.es

<sup>2</sup> Instituto Universitario Carlos I de Física Teórica y Computacional, Facultad de Ciencias, 18071 Granada, Spain  
e-mail: azurita@ugr.es

<sup>3</sup> Dpto. Física Teórica, Universidad Autónoma de Madrid, Cantoblanco, 28049 Madrid, Spain  
e-mail: p.sanchezblazquez@uam.es

Received 18 October 2011 / Accepted 24 April 2012

## ABSTRACT

**Aims.** This is the third paper of a series devoted to studying the properties of bars from long-slit spectroscopy to understand their formation, evolution, and influence on the evolution of disk galaxies. In this paper, we aim to determine the gas metallicity distribution of a sample of 20 barred early-type galaxies. We compare the nebular and stellar metallicity distributions to attempt to infer the origin of the warm gas.

**Methods.** We performed long-slit spectroscopy along the bar and obtained metallicities derived using different calibrations. We compare the nebular emission metallicities derived using different semi-empirical methods. We carry out AGN diagnostic diagrams for data at different radii to determine the radius of influence of the AGN and the nature of the galactic nuclei. We then derive the gas metallicities along the bars and compare our results to the distribution of stellar metallicities in the same regions.

**Results.** Most of the gas emission is centrally concentrated, although 15 galaxies also show emission along the bar. In the central regions, gas oxygen abundances are in the range  $12 + \log(\text{O}/\text{H}) = 8.4\text{--}9.1$ . The nebular metallicity gradients are very shallow in the bulge and bar regions. For three galaxies (one of them a low-ionization nuclear emission-line region), the gas metallicities lie well below the stellar ones in the bulge region. These results do not depend on the choice of semi-empirical calibration used to calculate the abundances. We see that the galaxies with the lowest metallicities are those with the largest rotational velocities. Unlike our stellar metallicities, we find no correlation between the nebular abundances and the central velocity dispersion. In most galaxies, the gradient in the gas nebular metallicities in the bulge region is shallower than that for the stellar metallicity.

**Conclusions.** The presence of gas of significantly lower metallicity than the stellar abundances in three of our galaxies, suggests that the gas has an external origin that fuels the present star formation at the center of some early-type barred galaxies. That the bar/disk nebular metallicities are higher than the central ones might indicate that the gas could be accreted via cooling flows instead of radial accretion from gas sitting in the outer parts of the disk.

**Key words.** galaxies: abundances – galaxies: evolution – galaxies: spiral

## 1. Introduction

With the exception of a few primordial light elements, stellar nucleosynthesis is responsible for the secular metal enrichment in galaxies. The final metallicity distribution within a galaxy is reasonably well-reproduced by chemical evolution models considering the appropriate star formation history together with episodes of gaseous inflow and outflows (e.g. Portinari & Chiosi 1999; Chiappini et al. 2000; Prantzos 2008; Colavitti et al. 2008). However, the metallicity gradients can be further modified by dynamical processes (e.g., Roskar et al. 2008; Schönric & Binney 2009; Sánchez-Blázquez et al. 2009). It is, therefore, evident that observing how metals are distributed in a galaxy should tightly constrain its evolution. However, the detailed dynamical processes responsible for the modification of the metallicity distribution and their importance remains poorly understood.

In particular, it is unknown, from the observational point of view, the importance that bars might have in producing the metallicity radial mixing. Bars are believed to affect the

overall dynamics of the galaxy and are a well-known mechanism to induce secular evolution (Athanasoula 2003; Pfenninger & Friedli 1991). For instance, in a previous study (Pérez & Sánchez-Blázquez 2011, hereinafter, Paper II) we hinted that the bulges of early-type barred galaxies have different stellar enrichment histories from the bulges of their unbarred counterparts (see also Ellison et al. 2011, for a similar conclusion for gas-phase metallicities).

Gas and stars respond to the gravitational potential according to their own nature, viscosity and magnetic fields only being important in the former component. The highly asymmetric bar potential induces differential radial motions. While the gas component, which is highly dissipative, is affected by the gravitational torque of the non-axisymmetric mass component, the stars are mainly affected by orbital mixing. Furthermore, studies of the gas-phase abundances provide present-day snapshots of the interstellar medium abundance. On the other hand, the study of stellar abundances provide archeological clues as to the formation and evolution of the bar. Therefore, studies of stellar and gas metallicities are of crucial importance to interpret the processes dominating galaxy evolution. It is expected that, if gas were injected into the interstellar medium (ISM) from stellar outputs, it would generally be more metal-rich than if it had an external origin.

\* Based on observations obtained at Siding Spring Observatory (RSAA, ANU, Australia) and the INT telescope at the ING, La Palma, Spain.

\*\* Figure 11 is available in electronic form at <http://www.aanda.org>

Deriving the disk radial distribution of stellar abundances from spectroscopic measurements is difficult owing to the low surface brightness of the disk and the contamination of the absorption lines by emission from ionised gas. Few works have tried to overcome these difficulties and have derived the radial distribution for only a small number of galaxies (e.g. Yoachim & Dalcanton 2008; MacArthur et al. 2009; Sánchez-Blázquez et al. 2011). The stellar metallicity gradients along the bars of the 20 early-type galaxies presented here were derived in previous works (Pérez et al. 2009, hereinafter, Paper I) and provided interesting results about the radial distribution of the stellar parameters in the bar region.

As for the nebular gas-abundance distribution, in most studied spiral galaxies, both barred and unbarred, negative radial metallicity gradients along the disk have been obtained for the gas component (e.g. Bresolin et al. 2009). These gradients seem to be shallower for barred than unbarred galaxies, but steeper for late-types than early-types (Pagel & Edmunds 1981; Alloin et al. 1981; Vila-Costas & Edmunds 1992; Zaritsky et al. 1994). The issue is not closed yet, so work is being done to investigate the variation in the gradient with radius (Bresolin et al. 2009 obtain a steeper gradient in the central part of M83, than in the outer disk, beyond  $1.2 R_{25}$ ) as well as in azimuth (Balsler et al. 2011, for the Milky Way). Simulations explain the shallower gradient in the outer than inner part of a galaxy based on radial mixing processes associated with a strong bar (e.g. Considere et al. 2000; Zahid & Bresolin 2011; Friedli et al. 1994; Friedli 1999). In this work, we focus on the analysis of the gas metallicity, in the bar region of the galaxies presented in Papers I and II.

Only a few works have considered both nebular and stellar metallicities. A pioneering study was presented by Storchi-Bergmann et al. (1994). They found a strong correlation between stellar and gas metallicity by investigating the correlation between the oxygen abundance in the nebular component, and the absorption-line equivalent width  $W(\text{CIV}\lambda 1550)$  (as a tracer of stellar metallicity) in a sample of 44 star-forming galaxies. They concluded that galaxies with lower values of metallicity appear to experience instantaneous outbreaks of star formation, but those with higher metallicity are probably undergoing stellar formation. Annibali et al. (2010) estimated the gas abundance gradients in early-type galaxies, comparing these results with their stellar metallicities (Annibali et al. 2007), and concluding that the gas metallicity tends to be lower than the stellar one, particularly at higher metallicities.

In this paper, we present an analysis of the radial oxygen abundance distribution in the bulge and bar regions of a sample of 20 early-type barred galaxies, with and without nuclear activity. The stellar component of this sample was studied in Papers I and II. In Sect. 2, observations and data reduction are described. The method to analyze the spectral lines to estimate their flux is presented in Sect. 3. In Sect. 4, we show the diagnostic diagrams and derive the abundance distributions with different methods. A comparison of the nebular and stellar metallicity gradients is also presented in this section. The results are discussed in Sect. 5.

## 2. Observations and data reduction

We obtained long-slit spectra along the bar major axis<sup>1</sup> for our sample of 20 barred galaxies. The observations were performed in two different runs, with the double beam spectrograph at Siding Spring Observatory (Australia, hereinafter, run1) and the

<sup>1</sup> The bar position angles were derived using the Digital Sky Survey (DSS) images.

IDS spectrograph at the *Isaac Newton* Telescope (La Palma, Spain, hereinafter, run2). The observations were described in detail in Paper I. To summarise, spectra for seven galaxies were obtained in the first run, covering a wavelength range from 3892–5815 Å and 5390–7314 Å with a spectral resolution of  $FHWM \sim 2.2$  Å. In spite of this overlap between both of these wavelength ranges, a relative calibration was impossible because the transmission of the dichroic gets as low as 50%, producing data of very low signal-to-noise ratio, and we have no bright lines in this region. In the second run, spectra for 13 galaxies were obtained, covering a wavelength range of 3020–6665 Å with a spectral resolution of  $\sim 3$  Å (FWHM), but the unvignetted range is 3600–6300 Å.

The seeing size during these observations ranges from 0.6'' to 1.2'' at the INT and from 1'' to 1.5'' at SSO. The characteristics of the sample were described in Papers I and II. For convenience, Table 1 shows the sample main properties.

Atmospheric dispersion can have important effects on spectrophotometry when the slit position angle differs from the parallactic angle during the observations. This is not so critical in our observations as we observed extended objects (diffuse emission or emission knots with sizes typically a few arcseconds larger than our slit width).

In any case, to be on the safe side, we kept the target airmass below 1.6 during the observations to ensure an atmospheric differential refraction between the lines of  $[\text{OII}]\lambda 3727$  Å and  $[\text{OIII}]\lambda 5007$  Å that is smaller than 1.5'' (Filippenko 1982). Differential atmospheric refraction between any other pair of lines involved in the empirical metallicity calibrations used in the paper is always smaller than the differential atmospheric refraction between  $[\text{OII}]\lambda 3727$  Å and  $[\text{OIII}]\lambda 5007$  Å.

For a few galaxies in which the difference between the bar position angle and the parallactic angle was greater than  $\approx 40$  deg, we tried to keep the airmass below 1.3 (which implies a differential atmospheric refraction between  $[\text{OII}]\lambda 3727$  Å and  $[\text{OIII}]\lambda 5007$  Å of  $\approx 1''$ ).

The reduction of the two runs was carried out with the package REDUCEME (Cardiel 1999) and IRAF tasks. Standard data reduction procedures (flat-fielding, cosmic ray removal, wavelength calibration, and sky subtraction) were performed. Error images were created at the beginning of the reduction and processed in parallel with the science images. For details about the reduction steps, we refer to Paper I.

## 3. Analysis

We observed 20 early-type barred galaxies. Nebular emission was detected in 19 of them. In NGC 2950, we detect no emission at all, and in NGC 4245 only at a galactocentric radius of 6 arcsec. In NGC 1832 and NGC 1530, we resolve knots of star formation (SF hereafter) at radius  $R \leq 0.25 R_{25}$  ( $R_{25}$  being the length of the projected major axis of a galaxy at the isophotal level 25 mag/arcsec<sup>2</sup> in the *B*-band). For the other 16 galaxies, we observe non-resolved emission extending at least along the bulge radius, i.e.  $R \leq 5''$ – $15''$  depending on the galaxy (Table 1). For seven galaxies (NGC 1433, NGC 1530, NGC 1832, NGC 2665, NGC 2935, NGC 3081, and NGC 4314) we also found knots of gas emission at larger radii, corresponding to one or several crowded H II regions.

To compare gas and stellar abundances, we extracted the spectra along the radius using the same binnings as in Paper I. These binnings were chosen to ensure errors smaller than 15% in most of the Lick/IDS indices. We also add apertures at larger

**Table 1.** General properties of the galaxy sample.

Object	Type	Bar class	Nuclear type	Inner morph.	$B$	$V_{\max, \text{gas}}$	$i$	Bar size	Bulge radius	Run
(1)	(2)	(3)	(4)	(5)	(6)	(7)	(8)	(9)	(10)	(11)
						(km s <sup>-1</sup> )	(deg)	(arcsec)	(arcsec)	
NGC 1169	SABb	3 <sup>a</sup>	(-)	-	12.35	259.1 ± 7.3	57.1	29	5	run2
NGC 1358	SAB(R)0	-	Sy2 (Sy2)	-	13.19	136.1 ± 10.6	62.8	-	5	run2
NGC 1433	(R)SB(rs)ab	4 <sup>b</sup>	LINER (Sy2)	Double-bar <sup>a</sup>	10.81	85.1 ± 2.4	68.1	-	5	run1
NGC 1530	SBb	6 <sup>b</sup>	(-)	-	12.50	169.1 ± 3.5	58.3	69	15	run2
NGC 1832	SB(r)bc	2 <sup>d</sup>	(-)	-	12.50	129.9 ± 2.0	71.8	-	7	run2
NGC 2217	(R)SB(rs)0/a	-	LINER (LINER?)	Double-bar <sup>b</sup>	11.36	183.4 ± 9.2	30.7	-	5	run1
NGC 2273	SB(r)a	2 <sup>c</sup>	Sy2 (Sy2)	-	12.62	192.2 ± 5.5	57.3	21	5	run2
NGC 2523	SBbc	-	(-)	-	12.64	211.4 ± 10.9	61.3	-	10	run2
NGC 2665	(R)SB(r)a	-	T (-)	-	12.47	130.9 ± 7.1	32.8	-	5	run1
NGC 2681	(R)SAB(rs)0/a	1 <sup>c</sup>	(LINER)	Triple-bar <sup>c</sup>	11.15	87.5 ± 6.7	15.9	23	8	run2
NGC 2859	(R)SB(r)0 ^	1 <sup>c</sup>	(Sy)	Double-bar <sup>d</sup>	11.86	238.5 ± 13.3	33.0	48	7	run2
NGC 2935	(R)SAB(s)b	-	T (-)	-	12.26	188.3 ± 2.0	42.7	-	7	run1
NGC 2950	(R)SB(r)0^0	-	(-)	Double-bar <sup>e</sup>	11.93	-	62.0	44	10	run2
NGC 2962	(R)SAB(rs)0	-	(-)	Double-bar <sup>c</sup>	12.91	202.9 ± 9.9	72.7	45	5	run2
NGC 3081	(R)SAB(r)0/a	3 <sup>c</sup>	Sy2 (Sy2)	Double-bar <sup>d</sup>	12.89	99.9 ± 4.0	60.1	35	5	run1
NGC 4245	SB(r)0/a	2 <sup>c</sup>	(-)	-	12.33	113.5 ± 5.4	56.1	59	6	run2
NGC 4314	SB(rs)a	3 <sup>a</sup>	LINER (LINER)	Double-bar <sup>c</sup>	11.42	253.3 ± 24.6	16.2	92	8	run2
NGC 4394	(R)SB(r)b	3 <sup>d</sup>	(LINER)	-	11.59	212.5 ± 16.0	20.0	56	5	run2
NGC 4643	SB(rs)0/a	3 <sup>c</sup>	LINER (LINER)	-	11.68	171.4 ± 7.2	42.9	67	10	run1
NGC 5101	(R)SB(r)0/a	2 <sup>d</sup>	LINER (-)	-	11.59	195.7 ± 9.0	23.2	-	7	run1

**Notes.** (1) Galaxy identification name. (2) Galaxy morphological classification. (3) Bar class derived from: <sup>(a)</sup> the  $K$ -band light distribution, Block et al. (2001); <sup>(b)</sup> the  $K$ -band light distribution, Block et al. (2004); <sup>(c)</sup> the  $K$ -band light distribution, Buta et al. (2006); <sup>(d)</sup> the  $H$ -band light distribution, Laurikainen et al. (2004). (4) Nuclear type, from this paper when possible. Between “( )” is the previous classification carried out by Veron-Cetty & Veron (2006).  $T$  is transition object. “-” means that no classification as an active galaxy was found in the literature. Low-Ionization Nuclear Emission-line Regions are labelled LINER. (5) Inner morphology, from <sup>(a)</sup> Buta (1986); <sup>(b)</sup> Jungwiert et al. (1997); <sup>(c)</sup> Erwin (2004); <sup>(d)</sup> Wozniak et al. (1995). (6), (7) and (8) Apparent total  $B$ -magnitude, maximum rotational velocity corrected for inclination and galaxy inclination, from the Hyperleda galaxy catalog. (9) Bar semi-major axis, from Paper II. (10) Bulge size, from Paper II. (11) run1 are galaxies observed at the SSO and run2 those observed at the INT.

radius to include those knots of star formation found in 7 of our galaxies (see above).

The gas emission-line fluxes were measured from the spectra after subtracting stellar templates. These stellar templates were obtained using GANDALF (Sarzi et al. 2005) and the set of stellar population models of Vazdekis et al. (2010) which makes use of the MILES library (Sánchez-Blázquez et al. 2006). After the stellar template subtraction, the spectra contains only the emission from the gas, with no contribution from the underlying stellar population. As representative examples, we show in Figs. 1–3 the central spectrum for three galaxies, two of run2 (one of them with weak emission and the other with stronger emission lines) and one of run1. They are shown before and after the template subtraction.

The emission-line fluxes were measured using the SPLLOT task in IRAF, by integrating the line intensity over a locally fitted continuum level. After marking two continuum points at both sides of the line, the flux was measured by taking into account the area, without any previous fitting of a Gaussian or any other assumed profile. Thus, asymmetries due to dynamical processes were indirectly considered. The corresponding uncertainties were estimated by adding in quadrature statistical errors measured by SPLLOT, flatfielding errors, and the error in the flux calibration. Typical errors are of order  $\sim 5\%$  (Table 2 shows the errors for the central apertures).

The observed line ratios relative to  $H\beta$  are afterwards corrected for interstellar reddening, by determining the reddening coefficient  $c(H\beta)$  through the expression

$$\frac{I(\lambda)}{I(H\beta)} = \frac{F(\lambda)}{F(H\beta)} 10^{c(H\beta)[f(\lambda)-f(H\beta)]}, \quad (1)$$

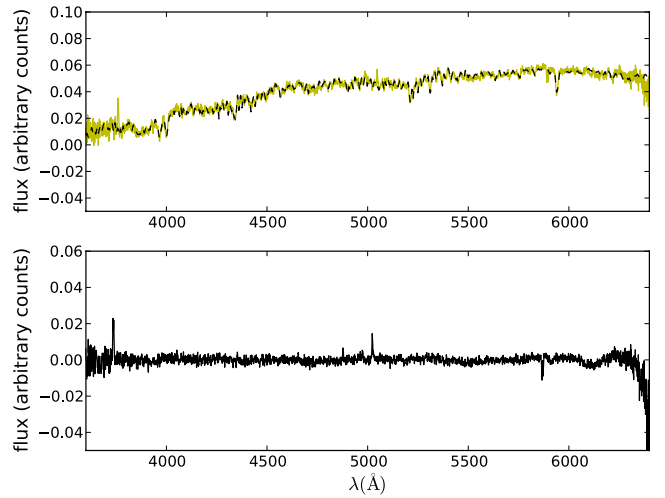


**Fig. 1.** Central spectrum for NGC 1169 (from run2). *The top panel* shows the observed spectrum (yellow line) and the fitted template (black line). *Bottom panel* shows the residuals from the fit. Oxygen and  $H\beta$  lines are clearly visible.

where  $f(\lambda)$  is the Seaton (1979) reddening curve parametrized by Howarth (1984), and  $I(\lambda)$  and  $F(\lambda)$  are the intrinsic and observed emission line flux at wavelength  $\lambda$ , respectively. We employ the Balmer lines detected within our spectral ranges. As explained in Sect. 2, both arms of the run1 observations were treated separately to avoid the introduction of an additional continuum scaling error, hence the  $H\alpha/H\beta$  was unavailable.

**Table 2.** Emission line strengths for the central aperture.

Galaxy	[O II] 3727	[Ne III] 3868	[O III] 4959	[O III] 5007	[N II] 6583	[S II] 6717	[S II] 6731
NGC 1169	525 ± 25	–	–	207 ± 10	–	–	–
NGC 1358	278 ± 13	65 ± 3	370 ± 18	1153 ± 55	–	–	–
NGC 1433	–	–	51 ± 2	155 ± 7	103 ± 6	34 ± 2	28 ± 2
NGC 1530	135 ± 40	–	–	23.5 ± 1.5	–	–	–
NGC 1832	28.6 ± 1.4	–	26.9 ± 1.3	33.5 ± 1.6	–	–	–
NGC 2217	–	–	100 ± 5	306 ± 14	226 ± 13	131 ± 11	115 ± 10
NGC 2273	168 ± 8	68 ± 3	237 ± 11	184 ± 9	–	–	–
NGC 2523	211 ± 10	–	194 ± 9	306 ± 15	–	–	–
NGC 2665	–	–	23 ± 1	72 ± 3	67 ± 3	19 ± 1	20 ± 1
NGC 2681	71 ± 3	–	105 ± 5	164 ± 8	–	–	–
NGC 2859	421 ± 20	–	99 ± 5	178 ± 8	–	–	–
NGC 2935	–	–	45 ± 2	128 ± 6	71 ± 3	24 ± 1	19 ± 1
NGC 2950	–	–	–	–	–	–	–
NGC 2962	399 ± 19	–	67 ± 3	174 ± 8	–	–	–
NGC 3081	–	84 ± 4	414 ± 20	1242 ± 60	88 ± 6	23 ± 1	21 ± 2
NGC 4245	–	–	–	–	–	–	–
NGC 4314	230 ± 11	–	93 ± 4	203 ± 10	–	–	–
NGC 4394	289 ± 14	–	108 ± 5	205 ± 10	–	–	–
NGC 4643	–	–	115 ± 5	73 ± 3	98 ± 12	31 ± 5	–
NGC 5101	–	–	86 ± 4	114 ± 5	189 ± 12	75 ± 7	59 ± 6

**Notes.** Emission line strengths for the central aperture of the galaxies, except for NGC 4314, which is at 0.8 arcsec from the galaxy center. The line fluxes of [O II], [Ne III], and [O III] lines are measured relative to a H $\beta$  flux of 100 and those of [N II] and [S II] lines are measured relative to a H $\alpha$  flux of 100.

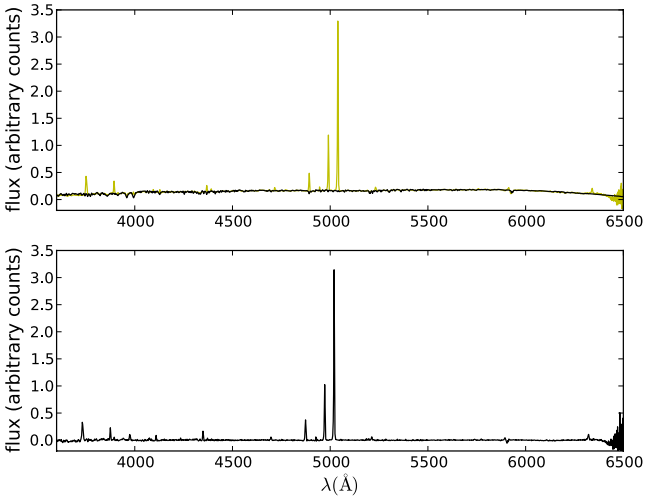


**Fig. 2.** Central spectrum for NGC 2273 (run2). Panels are the same as in Fig. 1. In this spectrum, the [Ne III]3868 line can be clearly identified.

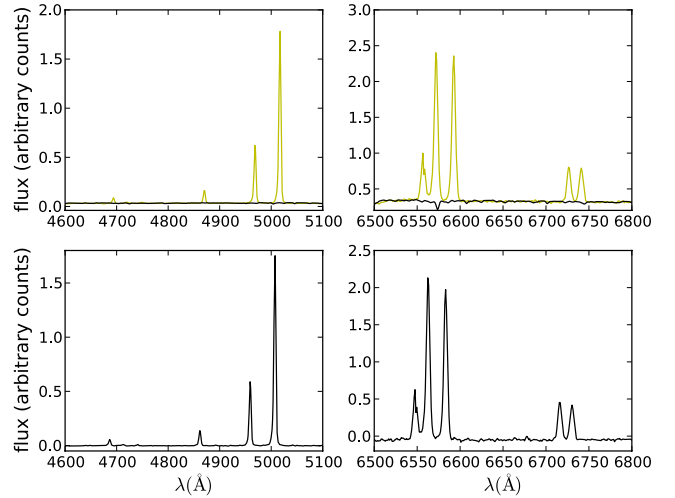


**Fig. 3.** Blue and red central spectra for NGC 3081 (run1). In the top panels, observed spectra (yellow lines) and templates (black lines) are shown. Bottom panels show the residuals of the fit.

The extinction constant was then obtained from the average of the extinction constant obtained by fitting all available Balmer line ratios relative to H $\beta$ , and the corresponding intrinsic or theoretical values. We considered the intrinsic flux ratio from Hummer & Storey (1987), assuming  $T_e = 10^4$  K and  $N_e = 100 \text{ cm}^{-3}$ . For these cases in which there is a high dispersion between the values for  $c(\text{H}\beta)$  obtained from different lines ratios, we used the extinction constant obtained from H $\gamma$ /H $\beta$  alone. We assigned an internal extinction of zero to objects for which the observed Balmer decrement was lower than the theoretical values. The derived reddening was negligible for most of the spectra. In the case of NGC 4245, we obtained only H $\beta$  and no other Balmer line, but did not consider this galaxy in the discussion. For NGC 1169, we observed only H $\beta$  except at five galactocentric radii. For four galaxies, the observed Balmer

decrement is lower than the theoretical one, so we consider as zero the internal extinction. In the fifth case, the obtained internal extinction is so low that the differences between the line fluxes, regardless of whether we consider this internal extinction, are lower than the obtained errors. Therefore, we assumed that there is negligible extinction in this galaxy.

Emission line strengths for the central aperture are shown in Table 2. For NGC 4314, we show the emission line strengths for the innermost aperture (0.8 arcsec from the galaxy center) with detected emission. This central aperture corresponds to 0.75 arcsec for run1 galaxies and 0.4 arcsec for run2 galaxies. Values of [O II], [Ne III], and [O III] are measured relative to H $\beta$  = 100, and those of [N II] and [S II] to H $\alpha$  = 100.

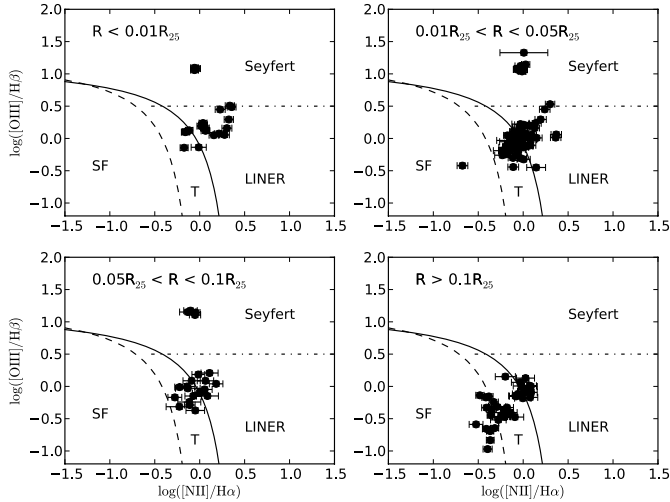


**Fig. 4.** Diagnostic diagram for the emission-line regions of run1 galaxies at different galactocentric distances ( $R$ ) scaled with  $R_{25}$ . The solid line (Kewley et al. 2001) sets the star formation upper limit, the dashed line (Kauffmann et al. 2003) the empirical division between star-forming galaxies (SF) and transition objects (T), and the horizontal line (Kewley et al. 2006) separates Seyferts and Low-Ionization Nuclear Emission-line Regions (LINERs).

For galaxies containing knots of gas emission, we also extracted spectra with apertures including all detected emission. In these cases, we corrected for extinction using an iterative method to determine, simultaneously, the underlying stellar absorption and interstellar reddening: we derived the extinction coefficient  $c(H\beta)$  for an assumed equivalent width of the stellar absorption  $EW_{\text{abs}}$  that was the same for all observed Balmer lines. The assumed  $EW_{\text{abs}}$  was varied until convergence between the  $c(H\beta)$  obtained from all the Balmer line ratios in use. The  $c(H\beta)$  values are in the range 0–2, and  $EW_{\text{abs}}$  was found to be in the range 0.7–1.8.

## 4. Results

### 4.1. Star formation versus nuclear activity

Once the line fluxes had been measured and extinction-corrected, we compiled diagnostic diagrams commonly used to distinguish between star formation (SF) regions and regions containing or affected by an active galactic nucleus (AGN). However, classical diagnostic diagrams ( $\log([O\text{III}]/H\beta)$  versus  $\log([N\text{II}]/H\alpha)$  and  $\log([O\text{III}]/H\beta)$  versus  $\log([S\text{II}]/H\alpha)$ ) (Baldwin et al. 1981; Veilleux & Osterbrock 1987) can only be applied to run1, owing to the limited spectral coverage of run2. For four galaxies, one from run1 and three from run2 we detected the  $[\text{Ne III}]\lambda 3868$  line. This line has been proposed as an empirical indicator of metallicity (Nagao et al. 2006) as well as a diagnostic to distinguish between starburst galaxies and AGNs (see discussion in Pérez-Montero et al. 2007).

Figures 4–6 present the diagnostic diagrams, in the first two figures at different galactocentric distances. In Fig. 4, we have plotted the theoretical curves of Kewley et al. (2001), which sets the maximum expected  $[O\text{III}]/H\beta$  at a given  $[N\text{II}]/H\alpha$  for a star-forming region, the curves of Kauffmann et al. (2003) that empirically divides star-forming galaxies from transition objects, and that of Kewley et al. (2006) separating Seyfert from low-ionization nuclear emission-line region (LINER) galaxies. In Fig. 5, we plot the relation between the

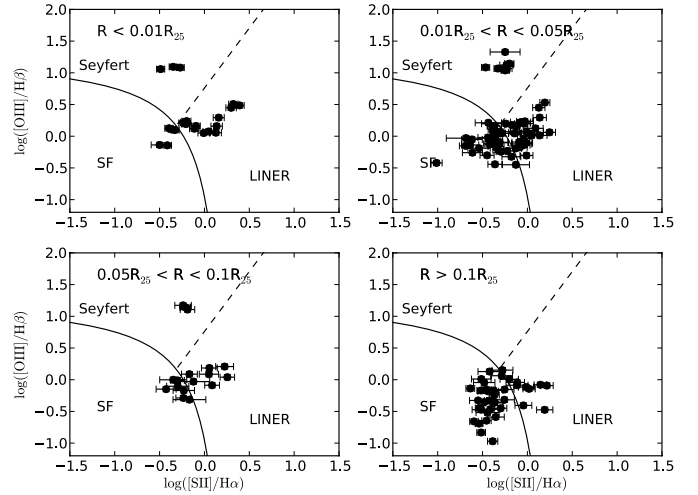


**Fig. 5.** Diagnostic diagram for the emission-line regions of run1 galaxies for different galactocentric distances ( $R$ ) scaled with  $R_{25}$ . The solid line delineates our adopted separation between star formation regions and AGNs; below the dashed line there are LINERs and above it Seyferts (Kewley et al. 2006).

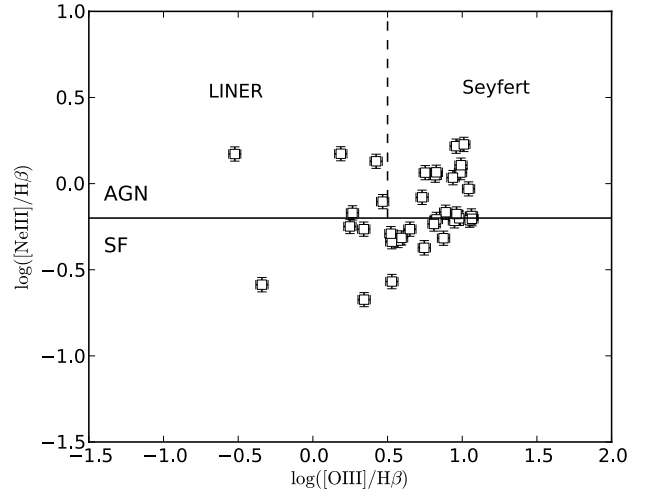


**Fig. 6.** Diagnostic diagram for those galaxies in which we have detected the  $[\text{Ne III}]\lambda 3869$  line. The solid line indicates the limit between star-formation regions and AGNs, and the dashed one between LINERs ( $[O\text{III}]\lambda 5007/H\beta \leq 0.5$ ) and Seyferts 2 ( $[O\text{III}]\lambda 5007/H\beta > 0.5$ ) (Rola et al. 1997).

line ratios  $\log([S\text{II}]/H\alpha)$  and  $\log([O\text{III}]/H\beta)$  for the galaxies in our sample at different radii. The theoretical models separating the values corresponding to ionization by star formation and AGN are also indicated. Rola et al. (1997) proposed an alternative diagnostic diagram based on the  $[\text{Ne III}]\lambda 3869$  line. In Fig. 6, this diagnostic diagram for galaxies in which we have detected this line is plotted, relating  $\log([\text{Ne III}]/H\beta)$  with  $\log([O\text{III}]/H\beta)$ . The solid line indicates the limit between star-formation regions and AGNs, and the dashed one between LINERs ( $[O\text{III}]\lambda 5007/H\beta \leq 0.5$ ) and Seyferts 2 ( $[O\text{III}]\lambda 5007/H\beta > 0.5$ ) as explained in Rola et al. (1997).

Figures 4 and 5 also show that at large radii, there is a higher probability that the gas is ionized by star-forming regions, while central emission is characterized by AGN-like line ratios.

Studying the diagnostic diagrams for individual galaxies, we confirm the classification carried out by Veron-Cetty & Veron (2006) with the exception of NGC 5101 and NGC 1433.

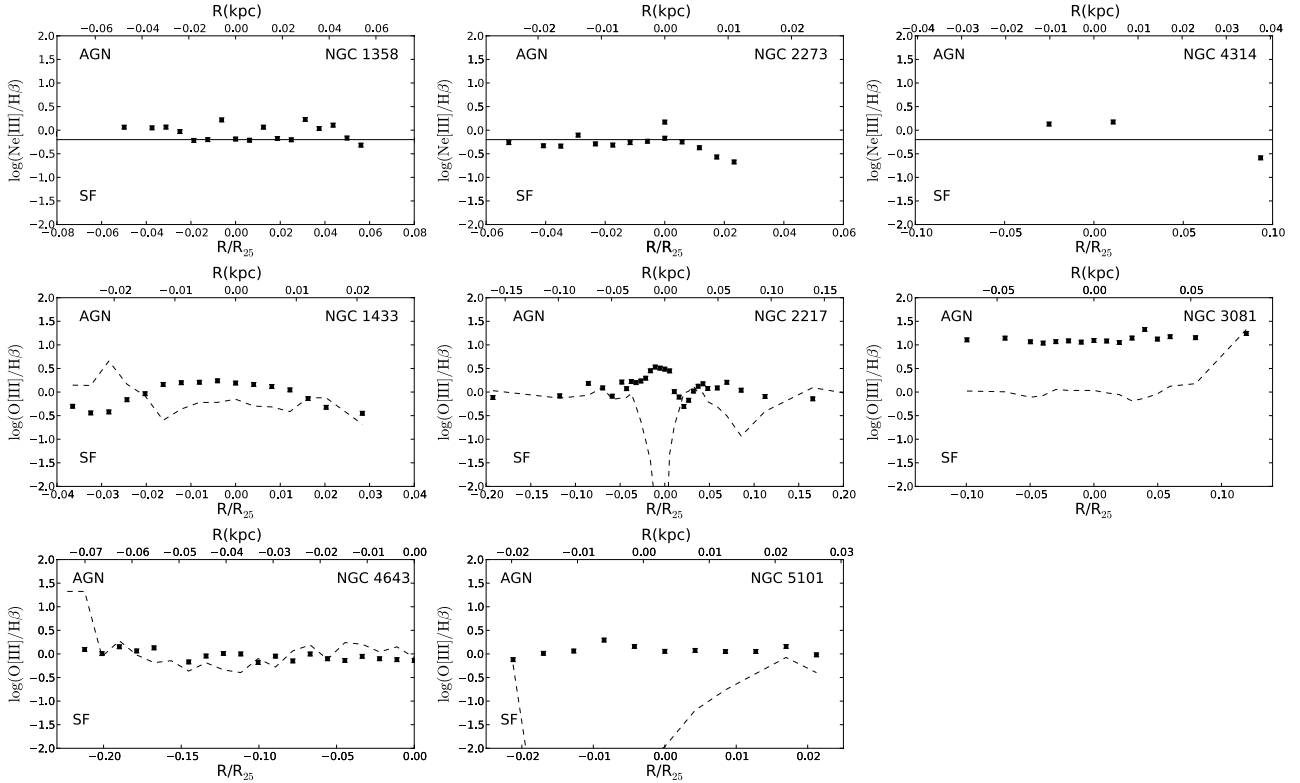


**Fig. 7.** Radial distribution of  $\log([\text{O III}]/\text{H}\beta)$  (for active galaxies of run1) and  $\log([\text{Ne III}]/\text{H}\beta)$  (for run2 galaxies with  $[\text{Ne III}]\lambda 3869$  line detected). The theoretical curves of Kewley et al. (2001, for  $\log([\text{O III}]/\text{H}\beta)$  and  $\log([\text{N II}]/\text{H}\alpha)$ ) and Rola et al. (1997, for  $\log([\text{Ne III}]/\text{H}\beta)$ ) distinguishing between AGN and SF are also plotted with dashed and solid lines, respectively.

According to the emission line in the central region, we reclassify NGC 5101 as a LINER even though it was not classified in this way in Veron-Cetty & Veron (2006). Our classification agrees with Moiseev (2001). The run1 galaxies that were not classified as Seyfert or LINER, NGC 2665, and NGC 2935, are transition objects. In Table 1, we compare the nuclear type obtained in this paper with that from a previous classification carried out by Veron-Cetty & Veron (2006).

Since we have radial information for the diagnostic diagrams, we considered the question of the AGN influence region by analyzing the radial behavior of the diagnostic ratios, to find the radius at which star formation starts being the main photoionisation source. Figure 7 shows the radial distribution of  $\log([\text{O III}]/\text{H}\beta)$  (or  $\log([\text{Ne III}]/\text{H}\beta)$ ). In the same figure, we have plotted the measured values of  $[\text{N II}]/\text{H}\alpha$ . With these values and taking into account the theoretical curve of Kewley et al. (2001) (or Rola et al. 1997 for  $\log([\text{Ne III}]/\text{H}\beta)$ ), we obtained the limiting for either star formation or nuclear activity, which are indicated by a dashed line. At a given galactocentric radius, if the observational points are above these lines, a star-forming region is not the main photoionization component at that radius. The AGN or LINER is the dominant ionization mechanism up to different radii for different galaxies: for example, for NGC 2273 evidence of the ionization by an AGN is present only at the smallest considered radii. For NGC 2217, the influence region of AGN extends to  $\sim 0.1$  kpc.

#### 4.2. Oxygen abundances and gradients

The measurement of nebular gas abundances has several difficulties. The *direct method* to calculate oxygen abundances involves the use of the ratios of temperature sensitive lines, such as

$[\text{O III}]\lambda\lambda 4959, 5007/\lambda 4363$  (Osterbrock 1989). Unfortunately, when the metallicity increases, the electronic temperature decreases and the auroral lines (e.g.  $[\text{O III}]\lambda 4363$ ) become too weak to be measured in most extragalactic objects, hence we have to find empirical, semiempirical, and theoretical calibrations to calculate abundances. Some relations between the gas metallicity and line flux ratios of strong emission lines have been found. A drawback of these indicators is that they have been basically developed for low-metallicity H II regions, where the  $[\text{O III}]\lambda 4363$  line is easily observed. However, it has been made considerable efforts to study high metallicity H II regions (e.g. Castellanos et al. 2002; Bresolin 2007), since these are the most abundant in early-type spiral galaxies and the central regions of late-type spiral galaxies (Vila-Costas & Edmunds 1992). Although semiempirical methods provide better results in statistical studies than individual values (Pérez-Montero et al. 2007), we used these methods to estimate the oxygen abundance variations with galactocentric radius. Systematic discrepancies among different methods have been found (see, for instance, Kewley & Ellison 2008; López-Sánchez & Esteban 2010, and references therein), so we used several methods to study the dependence of the results on the method chosen.

An additional problem is that 11 out of our 20 galaxies have been classified as either LINERs or Seyferts. The mechanism of ionization in the case of LINERs is still not well-understood, so there are no methods for estimating abundances in the central parts of these galaxies. Some methods exist in the case of Seyferts, but owing to our limited spectral coverage we can only apply one of them, and in some particular cases. We also apply this method in LINERs, powered by some process which may be in-between AGN excitation and photoionization due to star formation.

#### 4.2.1. Nebular abundances: errors in their determination and comparison between different methods

We use different methods to estimate the nebular abundances for the two different runs, as the spectral range covered in both data sets is different. The brightest lines measured, apart from the Balmer ( $H\gamma$ ,  $H\beta$ ,  $H\alpha$ ) lines are the  $[\text{O III}]\lambda\lambda 4959, 5007$ ,  $[\text{N II}]\lambda\lambda 6548, 6583$ , and  $[\text{S II}]\lambda\lambda 6717, 6731$  lines for run1 galaxies, and  $[\text{O II}]\lambda 3727$  and  $[\text{O III}]\lambda\lambda 4959, 5007$  for run2 galaxies. At some distances from the center,  $[\text{O III}]\lambda 4959$  is not detected, in which case we assume that  $[\text{O III}]\lambda\lambda 4959, 5007 = 1.337[\text{O III}]\lambda 5007$  (Oey & Kennicutt 1993).

The abundance indicators used in this work are:

1.  $R_{23}$ : on the basis of this parameter ( $R_{23} = ([\text{O III}]\lambda 3727 + [\text{O III}]\lambda\lambda 4959, 5007)/H\beta$ ), we use two calibrations:
  - M91: the theoretical calibration of McGaugh (1991), which takes into account the influence of the ionization parameter to determine the chemical abundance.
  - Z94: it is an analytical calibration derived by Zaritsky et al. (1994) from the average of three previous  $R_{23}$  calibrations (Dopita & Evans 1986; McCall et al. 1985; Edmunds & Pagel 1984). It is only valid for high metallicity objects with  $\log(\text{O}/\text{H}) + 12 > 8.35$ .
2.  $N2$ : this uses  $\left(\frac{[\text{N II}]\lambda 6583}{H\alpha}\right)$  (Pettini & Pagel 2004), which has the advantage of not being double-valued with oxygen abundance, and that lines are very near each other, minimizing the dependence on the reddening correction.
3.  $O3N2$ : this depends on  $\left(\frac{[\text{O III}]\lambda 5007/H\beta}{[\text{N II}]\lambda 6583/H\alpha}\right)$  (Pettini & Pagel 2004) and is a monotonic function of the oxygen abundance. However, in our present study, the pairs of lines ( $[\text{O III}]\lambda 5007, H\beta$ ) and ( $[\text{N II}]\lambda 6583, H\alpha$ ) are detected in separate spectra, which can introduce errors caused by a mismatch between the continuum fluxes in the red and blue (run1) ranges. This problem is discussed at the end of this section.
4.  $O2Ne3$ : Pérez-Montero et al. (2007) discussed the relation between  $[\text{Ne III}]\lambda 3869$  and  $[\text{O II}]$ , and defined the parameter  $O2Ne3 = \frac{I([\text{O II}]\lambda 3727) + 15.371([\text{Ne III}]\lambda 3869)}{I(H\beta)}$ . Taking into account this parameter, we calculated the oxygen abundance with the expression of M91. This line is more intense in AGNs because, in these objects,  $\text{Ne}^{+2}$  is less suppressed than in star-formation regions, as explained in Rola et al. (1997).
5.  $SBI$ : this was calibrated for active galaxies (Storchi-Bergmann et al. 1998) and has two different calibrations. It is valid for Seyfert galaxies but not so accurate for LINERs. We used the calibration involving the  $[\text{O III}]$ ,  $[\text{N II}]$ ,  $H\alpha$  and  $H\beta$  lines because of our observed spectral range, which depends on the gas density, and is valid only for  $100 < N < 10000$  (where  $N$  is the gas density in  $\text{cm}^{-3}$ ) and  $8.4 < 12 + \log(\text{O}/\text{H}) < 9.4$ .
6.  $KD02$ : this method was proposed by Kewley & Dopita (2002), which consists of an iterative scheme involving the ionization parameter and  $R_{23}$ .
7.  $P05$ : Pilyugin & Thuan (2005) improved the calibration of Pilyugin (2000, 2001) with a more extended (in metallicity) set of H II regions. The lines needed to measure this indicator are  $[\text{O II}]\lambda\lambda 3727, 3729, [\text{O III}]\lambda\lambda 4959, 5007$ , and  $H\beta$ .

We applied  $R_{23}$ ,  $O2Ne3$ ,  $KD03$ , and  $P05$  methods to galaxies observed in run2 and  $N2$ ,  $O3N2$ , and  $SBI$  to those observed in run1.

Several of the indices described above have two branches in their calibration, i.e., there are two possible metallicity values for a given index. This makes it necessary to have additional

criteria to distinguish between the upper and the lower branches. We adopt the high-metallicity values based on (a) the empirical diagrams of Nagao et al. (2006) (though not for active galaxies). With a sample of 50 000 spectra, they proposed a method based in the monotonic metallicity dependence of  $[\text{O III}]\lambda 5007/[\text{O II}]\lambda 3727$ , that enabled the  $R_{23}$  degeneracy to be broken. We made use of their diagrams to determine the branch. (b) The Kobulnicky et al. (1999) conclusion about galaxies in the local Universe (i.e. objects more luminous than  $M_B \sim -18$  have metallicities higher than 8.3, and the whole sample lies within this range). (c) Galaxy morphologies, all the galaxies being of early-type and Oey & Kennicutt (1993) found that the average metallicity value for H II regions in Sa and Sb galaxies is 8.97, clearly in the upper region. (d) In NGC 1530, this these high-metallicity values are similar to those found by Márquez et al. (2002) using the  $[\text{N II}]/H\alpha$  ratio. A special case is that of NGC 1358: the  $R_{23}$  values calculated for this galaxy are in the limit of applicability of the methods based on this parameter. However, using data for  $[\text{N II}]$  and  $H\alpha$  we calculated abundance values consistent with these obtained using the  $R_{23}$  method.

The errors in the oxygen abundances were estimated by means of the error propagation of the uncertainties in the relevant line fluxes and range between  $\sim 0.01$  and  $0.10$  dex (or 10–20% in  $[\text{O}/\text{H}]$ ). This is smaller than the intrinsic scatter associated with the empirical calibrations of the so-called strong-line methods (e.g. 0.2 dex for  $R_{23}$ , Athey & Bregman 2009). We carried out various tests to determine the uncertainties introduced into the different parts of the analysis. Abundances were estimated in two possible ways for each test of this analysis. In what follows, we describe the maximum differences found and the mean values of these differences in a galaxy chosen as a characteristic example:

- (a) As discussed in Sect. 3, in most of the spectra we used stellar templates to subtract the contribution from the underlying stellar population, an approach that provides a second way to correct the line intensities with an iterative method. The differences found in the gaseous abundances between both methods are smaller than 0.1–0.2 dex. As an example, for NGC 1433 the mean values of these differences are  $0.04 \pm 0.06$  dex for  $N2$ ,  $0.05 \pm 0.03$  dex for  $O3N2$ , and  $0.04 \pm 0.02$  dex for  $SBI$ .
- (b) Considering either an equivalent width due to Balmer absorption of  $2 \text{ \AA}$  to correct the stellar absorption, a typical value used in the literature (e.g. Zaritsky et al. 1994), or using the iterative method to estimate it, introduces differences smaller than 0.1–0.2 dex. For example, in NGC 1530 the mean values of these differences are  $0.04 \pm 0.04$  dex ( $R_{23}$ ),  $0.05 \pm 0.04$  dex ( $Z94$ ),  $0.03 \pm 0.02$  dex ( $KD03$ ), and  $0.13 \pm 0.09$  dex ( $P05$ ).
- (c) The error introduced if we were to consider an  $I(H\alpha)/I(H\beta)$  value of either 2.85 or 3.1 is as small as 0.05 dex. Annibali et al. (2010) also showed that, in any case, considering  $H\alpha/H\beta = 2.85$  does not significantly change the results. For NGC 3081, mean differences are  $0.0004 \pm 0.0008$  dex ( $N2$ ),  $0.003 \pm 0.004$  dex ( $O3N2$ ), and  $0.08 \pm 0.09$  dex ( $SBI$ ).

We next show that differences among the different metallicity calibrations are larger than these errors.

We compare the results from the different methods in Fig. 8, taking  $N2$  as a reference for run1 galaxies, and  $R_{23}$  (M91) for run2 galaxies. The values of  $O2Ne3$  could only be calculated for three galaxies; its behavior is the same as the  $R_{23}$  (M91) but has a larger dispersion. The measurement for  $R_{23}$  ( $Z94$ ) is

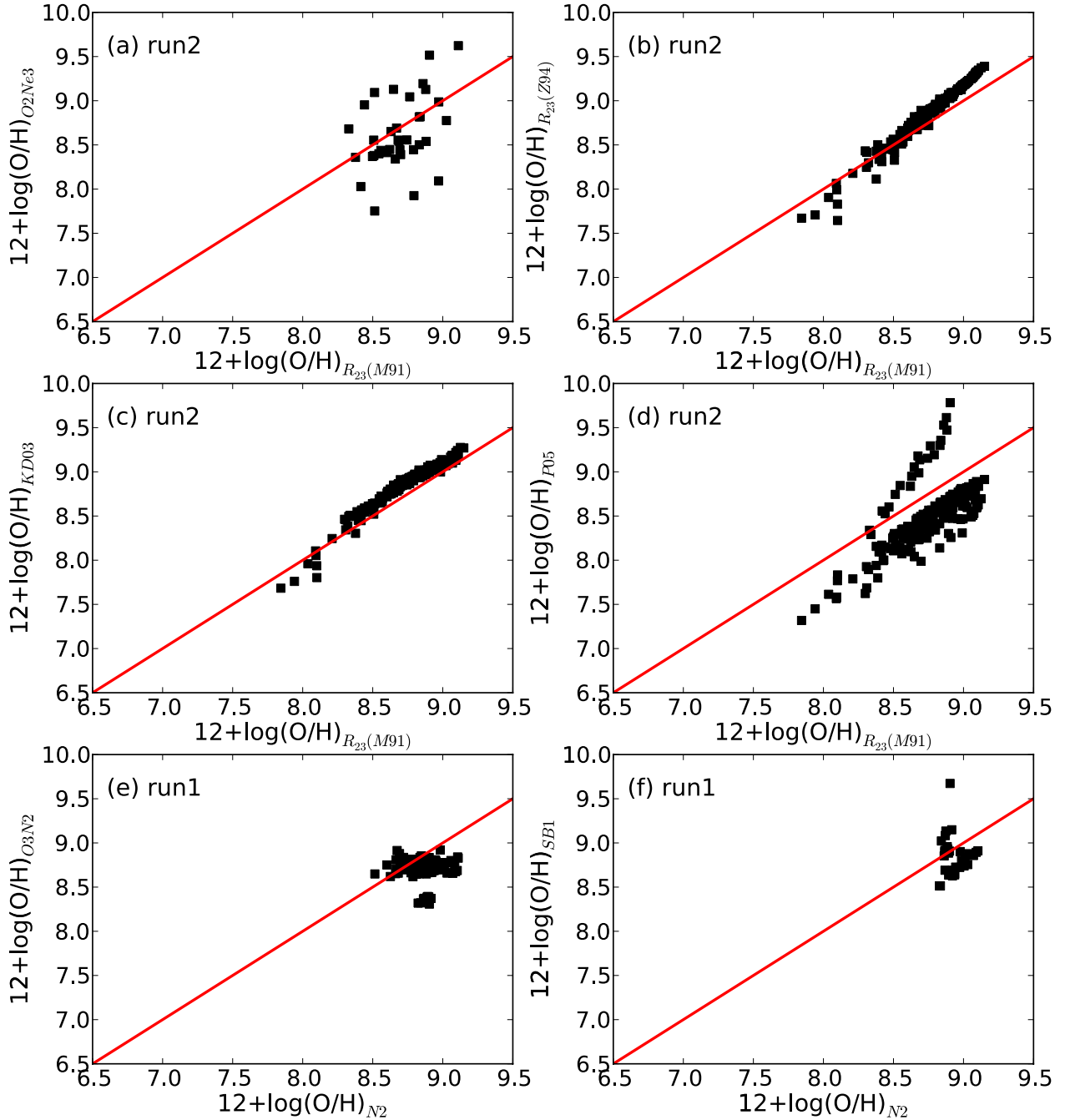


**Fig. 8.** Relation between different calibrations for obtaining oxygen abundances. In panels **a)–d)**, we compare the methods used for run2 galaxies with the  $R_{23}$  calibration by McGaugh (M91). In panels **e)** and **f)**, the comparison is for run1 galaxies, between  $\text{N2}$  and either  $\text{O3N2}$  or  $\text{SBI}$ . The solid line in each plot shows the agreement between the different methods.

valid for  $12 + \log(\text{O}/\text{H}) > 8.35$  (Zaritsky et al. 1994). For  $12 + \log(\text{O}/\text{H})$  values between 8.35 and 8.7, the  $R_{23}$  method, with the calibrations of Z94 and M91, provide similar metallicity values, but from 8.7 upwards, the Z94 value becomes higher than the M91 one. In  $\text{KD03}$ , the behavior is the same as in  $R_{23}$  (M91), but  $\text{KD03}$  gives values slightly above those of  $R_{23}$  (M91) from 8.2 upwards. The  $\text{P05}$  values are systematically 0.3–0.5 dex lower than those of  $R_{23}$  (M91) with the exception of NGC 1358. Bresolin et al. (2009) showed that, for the external parts of the disk of M83, the variation in metallicity with  $[\text{N II}]/[\text{O II}]$  is closer to the actual values, being 0.4 dex lower than those obtained with  $R_{23}$ . Therefore, the metallicities derived using the  $\text{P05}$  method might be expected to be more

realistic or, at least, closer to the direct metallicity determinations. Kennicutt et al. (2003) found systematic differences of up to 0.5 dex between the  $T_e$  and  $R_{23}$  abundances. Pilyugin & Thuan (2005) noted that the determination of oxygen abundances using  $\text{P05}$  agrees with the  $T_e$  abundance to within 0.1 dex, even at high metallicity, as in our case.

For run1 galaxies, the largest differences between  $\text{O3N2}$  and the  $\text{N2}$  index are 0.3–0.4 dex, except for NGC 3081, for which the difference is around 0.5 dex. Denicoló et al. (2002) emphasized the importance of the  $\text{N2}$  method, showing that the  $\text{O3N2}$  calibration did not improve the results. We note that  $\text{SBI}$  is a method calibrated for AGN; though 11 of the galaxies studied here have been classified as active, this method has only

been used in the cases that meet the above conditions of density and metallicity, and only to run1 galaxies because of the lines involved.

It is interesting to compare the radial dependence of the values obtained with the different methods, to study either the effect of nuclear activity or the differences due to the physical differences between the nuclear and disk H II region properties. The H II characteristics can influence the abundance trends obtained using different methods in different ways (Kennicutt et al. 1989). The systematic differences are presented later in our comparison with stellar metallicities. Figure 9 shows the residual values of the different abundance-calculation methods for all the galaxies with respect to  $R_{23}$  (M91) for run2 galaxies and  $N2$  for run1 galaxies.

As already noted, our  $P05$  abundances are always below  $R_{23}$  (M91), the difference being around 0.5 dex, without any variation with radius (with the exception of the special case NGC 1358 as we have mentioned). For  $KD03$ , the largest differences are found in the central part of the Seyfert galaxy NGC 1358, which are much smaller outside radii of  $0.08 R/R_{25}$ , indicated as the activity zone in Fig. 7. However, this is not the result typically found for Seyferts (see NGC 2273), for which we personally find similar values to those calculated with  $R_{23}$  calibrations by M91 and Z94. We find a larger dispersion for  $O2Ne3$  than for the other methods, without any systematic trend with radius, the largest deviation occurring for galaxies that have fewer radial bins (e.g. NGC 4314). Between  $O3N2$  and  $N2$ , the differences are small in most galaxies, less than 0.2–0.3 dex. However, for two galaxies, NGC 3081 and NGC 2217, these differences are larger (0.4–0.5 dex), but then become smaller (again 0.1–0.2 dex) with radius, at larger galactocentric distances.

As above mentioned, 11 galaxies have been classified as Seyferts or LINERs. All methods used here to derive metallicity, with the exception of  $SB1$ , have been derived for star-forming galaxies. We can only use the specific calibration method  $SB1$  in 3 of our 20 galaxies, NGC 1433, NGC 2217, and NGC 3081, even though only one of these, i.e. NGC 3081, is clearly a Sy2. Annibali et al. (2010) compared oxygen abundances estimated from a photoionization model based on  $R_{23}$  (Kobulnicky et al. 1999) with  $SB1$ . The values obtained from the  $SB1$  method are on average  $\sim 0.04$  dex higher than those for the  $R_{23}$  calibration, but the differences between both metallicity values in individual regions can be as large as 0.3 dex. Keeping this result in mind, we have opted to show the values obtained with all the methods for comparison. This can be specially useful in the case of LINERs, whose mechanism of ionization is unknown. Therefore, we have calculated the abundance values with  $SB1$  whenever possible. For the active galaxies for which this method cannot be used, we only indicate the metallicities obtained from methods calibrated for star-forming regions, and we caution the reader again about the validity of these values for AGN-dominated regions.

#### 4.2.2. Gas oxygen-abundance in barred galaxies

Figure 10 shows the oxygen abundances obtained with  $R_{23}$  (M91) or  $O3N2$  versus radii for all galaxies. We have linear fits performed in the bar region and in the bulge region taking into account the errors derived from the line fluxes.

Tables 3 and 5 show, respectively, for run2 and run1, the value of oxygen abundances within an aperture of 1.2 arcsec (i.e. after averaging abundances within the central 1.2 arcsec), the central abundance inferred by extrapolating to  $R = 0$  the

linear fit (for only  $R_{23}$  (M91) and  $O3N2$ ), and the central value from the extrapolation to  $R = 0$  excluding the region of influence of the AGN. Tables 4 and 5 show gradients for all used methods (in units of dex/arcsec), taking into account all the nebular emission in the bar region and their errors. Galaxies classified as either Seyferts or LINERs are marked with a dagger. For the galaxies for which we have enough points, we have two rows in these tables: the first one shows values obtained in the bar region, and the second those obtained excluding the AGN-affected region determined in the previous section. These regions affected by an AGN have been determined from Fig. 7, except for NGC 2681, NGC 2859, and NGC 4394 for which we have considered the radial ranges reported by Véron-Cetty & Véron (2006) and references therein. The numerical values are shown in Tables 3 and 5.

The seeing size could introduce errors in our measurements of the gradients. To study this effect, we produced artificial spectra at each pixel position, which we then convolved with Gaussians of different widths, covering the seeing values of these observations. This procedure was performed using the IRAF GAUSS task. We then generated three spectra. The largest differences in abundances calculated for these three spectra are smaller than 0.2, implying that the differences in the gradients are of  $\sim 5\%$ .

We analyzed our results using the indices  $R_{23}$  (M91) and  $O3N2$ . For run2 galaxies, differences are nearly constant at all radii, in such a way that gradients maintain their sign in nearly all methods. In run1 galaxies, there are variations with galactocentric distance as mentioned above. In particular, the three galaxies for which we applied the  $SB1$  method are also the galaxies with the largest differences in abundances in the central region, which are lower for  $O3N2$  than for  $N2$ . This difference does not persist to larger radii, so the gradient sign is opposite for the two methods. The oxygen abundances in a 1.2 arcsec aperture are in the range 8.4–9.1 dex.

If we consider all the detected emission in the bar region at a  $3\text{-}\sigma$  significance, for the star-formation galaxies, we detect a positive gradient for three galaxies (NGC 1169, NGC 2523, and NGC 2935) and a negative gradient for two galaxies (NGC 1832 and NGC 2962). For LINERs, we find a positive gradient for three galaxies (NGC 1433, NGC 4314, and NGC 4394) and none of them have a negative gradient. We find that for the region unaffected by any AGN that may be present in these galaxies, the sign of the gradients does not vary. In the case of Seyferts, we find negative gradients in four galaxies when we consider the bar region, but when we exclude the AGN-affected region, three of them keep their gradient sign. Only one of the Seyfert galaxies has a positive gradient, which is unaffected by the AGN region.

In most disks of spiral galaxies, both barred or unbarred, negative metallicity gradients have been obtained (e.g. Bresolin et al. 2009; Garnett & Shields 1987, etc.). This gradient seems to be shallower for barred than unbarred galaxies, and higher for late-type than for early-type galaxies (Hidalgo-Gómez et al. 2011; Vila-Costas & Edmunds 1992; Zaritsky et al. 1994). All our galaxies are barred and early-type; hence, based on previous studies, the gradient should be shallow. We find gradients in the range  $[-3.7, 1.4]$  (normalized to  $R_{25}$ ) with the exception of NGC 1169, which has a very large dispersion in its abundance values. In Sect. 5, we compare these values with those found in the literature.

In Tables 6 and 7, we present the obtained gradients for the bulge region for all adopted methods, and the central oxygen abundance (only with  $R_{23}$  (M91) or  $O3N2$  method). In these tables, we have marked the active galaxies but the gradients are

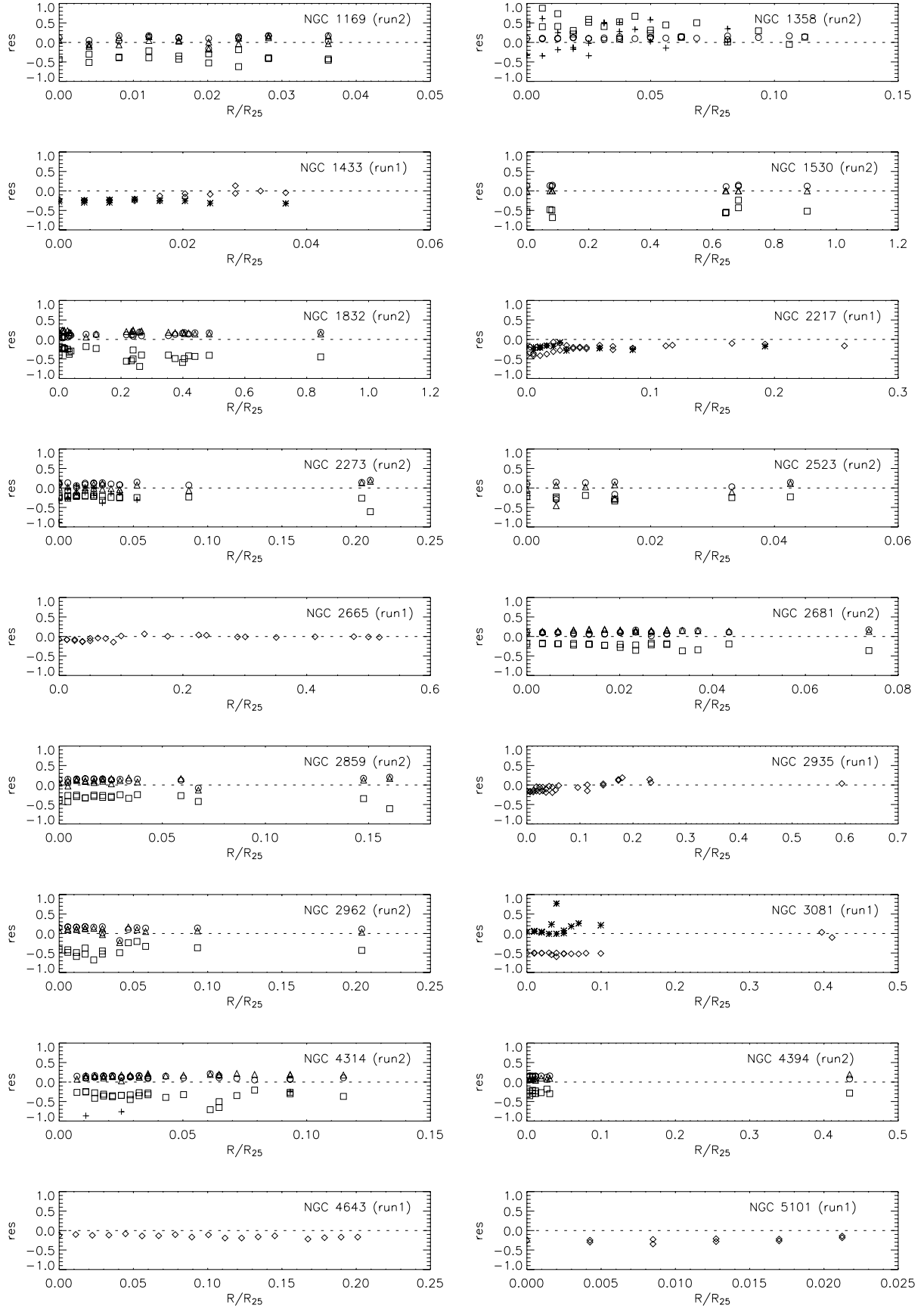


**Fig. 9.** Differences between the oxygen abundances obtained with the different methods versus the galactocentric radius for each galaxy.  $R_{25}$  has been taken from HyperLeda. Residuals are with respect to  $R_{23}$  (M91) for run2 galaxies and to  $N2$  for run1 galaxies. Crosses are oxygen abundances obtained from the  $O2Ne3$  calibration, triangles from  $R_{23}$  (Z94), circles from  $KD03$ , squares from  $P05$ , diamonds from  $O3N2$ , and asterisks from  $SB1$ .

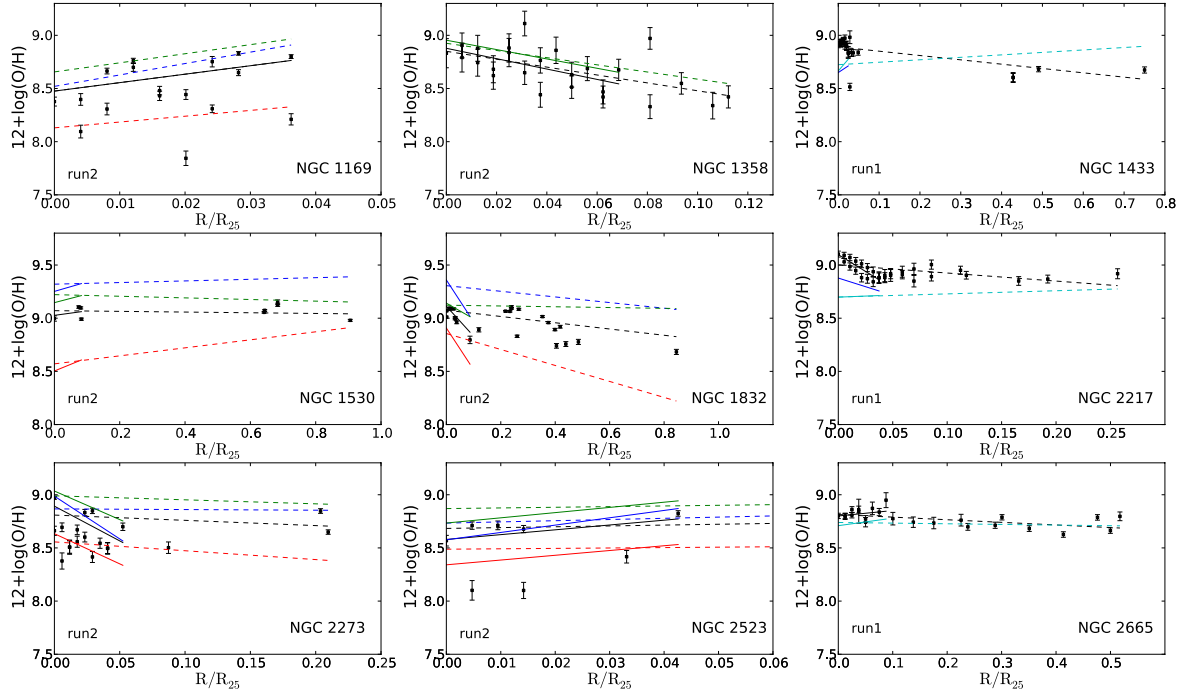


**Fig. 10.** Oxygen abundances of  $12 + \log(\text{O}/\text{H})$  obtained with  $O3N2$  for run1, and with  $R_{23}$  (M91) for run2, versus  $R/R_{25}$  in each galaxy. Dashed lines indicate the fits to all measured values, and solid lines show the best fits within the bulge region. For run1 galaxies, black lines indicate the  $N2$  fit, cyan lines the  $O3N2$  fit, and blue line the  $SBI$  fit. For run2 galaxies, black lines show the  $R_{23}$  (M91) fit, blue lines the  $Z94$  fit, green lines the  $KDO3$  fit, and red lines the  $P05$  fit.

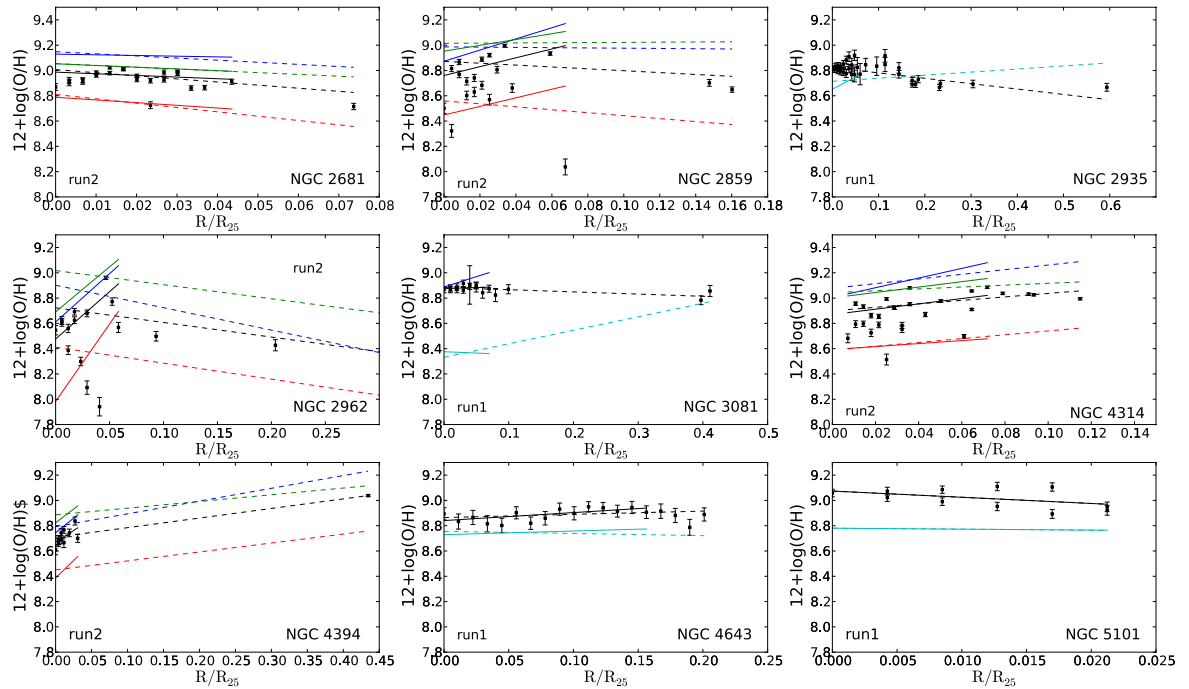


**Fig. 10.** continued.

fitted including the AGN regions. NGC 3081 is the only Seyfert galaxy for which we have been able to calculate abundances with the  $SBI$  method. For two galaxies (NGC 1169 and NGC 5101), all the measured nebular emission in the bar position is in the bulge zone where the scatter is larger than in the bar region and, therefore, errors are also larger. We find the same sign for the slopes in most of the star-forming galaxies. They are in general steeper than those measured when the bar region is considered.

#### 4.3. Comparison of the nebular gas abundances with the distribution of stellar metallicities

While measurements of the ionised gas abundances give information about the current composition of the ISM, the stellar metallicities are directly linked to the star formation history and, thus, a comparison between the metal abundances of both components can help us to determine the origin of the gas involved in the present star formation.

**Table 3.** Central abundances, for run2 galaxies.

Galaxy	$12 + \log(\text{O}/\text{H})^1$ dex	$12 + \log(\text{O}/\text{H})^2$ dex	$12 + \log(\text{O}/\text{H})^3$ dex	$R_{25}^4$ arcsec	AGN <sup>5</sup> arcsec
NGC 1169	$8.47 \pm 0.10$	$8.47 \pm 0.01$		99.34	
NGC 1358 <sup>†</sup>	$8.78 \pm 0.07$	$8.85 \pm 0.04$	$8.71 \pm 0.12$	64.14	3.2
NGC 1530	$8.90 \pm 0.02$	$9.071 \pm 0.006$		54.59	
NGC 1832	$9.09 \pm 0.01$	$9.075 \pm 0.003$		73.64	
NGC 2273 <sup>†</sup>	$8.57 \pm 0.05$	$8.809 \pm 0.008$	$8.828 \pm 0.009$	68.72	0.4
NGC 2523	$8.48 \pm 0.05$	$8.50 \pm 0.10$		84.55	
NGC 2681 <sup>†</sup>	$8.92 \pm 0.02$	$9.007 \pm 0.007$	$9.12 \pm 0.02$	119.43	3*
NGC 2859 <sup>†</sup>	$8.66 \pm 0.03$	$8.872 \pm 0.007$	$9.05 \pm 0.01$	94.87	3*
NGC 2962	$8.58 \pm 0.03$	$8.72 \pm 0.01$		68.72	
NGC 4314 <sup>†</sup>	$8.81 \pm 0.02$	$8.900 \pm 0.004$	$8.965 \pm 0.008$	111.46	3.3
NGC 4394 <sup>†</sup>	$8.69 \pm 0.03$	$8.708 \pm 0.009$	$8.67 \pm 0.02$	104.02	3*

**Notes.** <sup>(†)</sup> Active galaxies. <sup>(1)</sup> Central oxygen abundance in the gas, estimated within an aperture of 1.2 arcsec, and calculated with the  $R_{23}$  (M91) method. <sup>(2)</sup> Central oxygen abundance in the gas, as a result of the fit, calculated with the  $R_{23}$  (M91) method. <sup>(3)</sup> Central oxygen abundance in the gas, as a result of the fit outside the region affected by an AGN, calculated with the  $R_{23}$  (M91) method. <sup>(4)</sup>  $R_{25}$  is from the Hyperleđa galaxy catalogue. <sup>(5)</sup> AGN-affected region, in arcsec, obtained from Fig. 7 except those marked with \*, which were taking from Véron-Cetty & Véron (2006) and references therein.

**Table 4.** Oxygen abundance gradients for all adopted methods and the central abundance, for run2 galaxies.

Galaxy	grad- $R_{23}$ (M91) dex/arcsec	grad- $O2Ne3$ dex/arcsec	grad- $R_{23}$ (Z94) dex/arcsec	grad- $KD03$ dex/arcsec	grad- $P05$ dex/arcsec
NGC 1169	$0.080 \pm 0.007$	–	$0.108 \pm 0.015$	$0.086 \pm 0.012$	$0.055 \pm 0.013$
NGC 1358 <sup>†</sup>	$-0.058 \pm 0.017$	$0.04 \pm 0.03$	$0.11 \pm 0.01$	$-0.05 \pm 0.01$	$-0.12 \pm 0.05$
	$-0.03 \pm 0.02$	$0.06 \pm 0.08$	$0.05 \pm 0.03$	$-0.03 \pm 0.02$	$-0.08 \pm 0.10$
NGC 1530	$-0.0006 \pm 0.0002$	–	$0.0014 \pm 0.0002$	$-0.0014 \pm 0.0003$	$0.0069 \pm 0.0002$
NGC 1832	$-0.0040 \pm 0.0002$	–	$-0.0036 \pm 0.0003$	$-0.0005 \pm 0.0002$	$-0.0102 \pm 0.0002$
NGC 2273 <sup>†</sup>	$-0.0072 \pm 0.0013$	$-0.01 \pm 0.02$	$-0.001 \pm 0.002$	$-0.0055 \pm 0.0015$	$-0.012 \pm 0.002$
	$-0.009 \pm 0.001$	$-0.07 \pm 0.02$	$-0.004 \pm 0.002$	$-0.006 \pm 0.001$	$-0.014 \pm 0.002$
NGC 2523	$0.0093 \pm 0.0004$	–	$0.0133 \pm 0.0008$	$0.0073 \pm 0.0005$	$0.0045 \pm 0.0007$
NGC 2681 <sup>†</sup>	$-0.020 \pm 0.002$	–	$-0.014 \pm 0.004$	$-0.012 \pm 0.001$	$-0.029 \pm 0.003$
	$-0.046 \pm 0.005$	–	$-0.051 \pm 0.009$	$0.010 \pm 0.004$	$-0.074 \pm 0.008$
NGC 2859 <sup>†</sup>	$-0.0078 \pm 0.0013$	–	$-0.001 \pm 0.003$	$0.000 \pm 0.002$	$-0.012 \pm 0.003$
	$-0.027 \pm 0.002$	–	$-0.028 \pm 0.004$	$-0.020 \pm 0.003$	$-0.038 \pm 0.003$
NGC 2962	$-0.017 \pm 0.002$	–	$-0.026 \pm 0.004$	$-0.016 \pm 0.004$	$-0.018 \pm 0.003$
NGC 4314 <sup>†</sup>	$0.0123 \pm 0.0007$	$0.111 \pm 0.014$	$0.0165 \pm 0.0014$	$0.0066 \pm 0.0007$	$0.0136 \pm 0.0012$
	$0.005 \pm 0.001$	–	$0.0016 \pm 0.0019$	$0.0015 \pm 0.0012$	$0.0046 \pm 0.0016$
NGC 4394 <sup>†</sup>	$0.0073 \pm 0.0003$	–	$0.0097 \pm 0.0005$	$0.0051 \pm 0.0003$	$0.0068 \pm 0.0004$
	$0.0080 \pm 0.0008$	–	$0.0104 \pm 0.0014$	$0.006 \pm 0.001$	$0.0084 \pm 0.0012$

**Notes.** <sup>(†)</sup> Active galaxies (Seyferts and LINERs): the first row shows values calculated with all points, and the second one those calculated for radii outside the AGN-affected region.

In previous works (Pérez et al. 2007, 2009; Pérez & Sánchez-Blázquez 2011), we derived the radial distribution of the stellar ages and metallicities along the bar and the bulges of the galaxies presented in this work. Line strength indices were measured and used to derive age and metallicity gradients in the bulge and bar region by comparing with stellar population models.

Figure 11 shows the comparison of the stellar and ionized gas abundances along the radius for all the galaxies. For the sake of clarity, the radius is on a logarithmic scale and  $R = 0$  is shifted to  $\log(R) = -0.5$ . For run2 galaxies, the  $R_{23}$  (M91) calibration has been chosen, covering the error bars the values obtained with all methods with the exception of  $O2Ne3$ . The values obtained with all methods have been represented in the case of run1 galaxies. For the comparison, we have assumed as reference the solar value  $12 + \log(\text{O}/\text{H})_{\odot} = 8.69$  (Allende-Prieto et al. 2001)

and  $[\text{Fe}/\text{H}]$  for both components. We have indicated by a vertical line the influence region of any active nuclei. In this way, we again caution (Sect. 4.2.1) the reader that may be incorrect to compare the gas abundances with the stellar metallicities in the regions dominated by an AGN.

For the following run2 galaxies, the nebular metallicities lie clearly below the stellar metallicity values: NGC 1169, NGC 2962 (in agreement with Marino et al. 2011), and NGC 4394. Only NGC 4394 is classified as a LINER. This lower metallicity gas (w.r.t. the stellar metallicity) is located in the bulge region, and similar values for the metallicity of both components are found elsewhere. For run1 galaxies, nebular metallicities obtained with  $O3N2$  are lower than stellar metallicities in NGC 2217, NGC 3081, and NGC 4643. However, with the values obtained with  $N2$ , they are very similar (NGC 3081 and NGC 4643) or even higher (NGC 2217). These three galaxies

**Table 5.** Oxygen abundance gradients derived using all adopted methods, for run1 galaxies.

Galaxy	grad- <i>N2</i> dex/arcsec	grad- <i>O3N2</i> dex/arcsec	grad- <i>SBI</i> dex/arcsec	$12 + \log(\text{O}/\text{H})^1$ dex	$12 + \log(\text{O}/\text{H})^2$ dex	$R_{25}^3$ arcsec	AGN arcsec
NGC 1433 <sup>†</sup>	$-0.0022 \pm 0.0002$	$0.0012 \pm 0.0002$	$0.01 \pm 0.01$	$8.68 \pm 0.03$	$8.724 \pm 0.008$	184.98	
	$-0.0014 \pm 0.0002$	$0.0009 \pm 0.0002$			$8.77 \pm 0.01$		3.7
NGC 2217 <sup>†</sup>	$-0.0054 \pm 0.0009$	$0.0021 \pm 0.0008$	$-0.023 \pm 0.007$	$8.674 \pm 0.03$	$8.699 \pm 0.009$	140.32	
	$0.0004 \pm 0.0025$	$-0.0002 \pm 0.0009$			$8.76 \pm 0.03$		16.8
NGC 2665	$-0.0041 \pm 0.0006$	$-0.0010 \pm 0.0006$	–	$8.718 \pm 0.03$	$8.739 \pm 0.009$	59.86	
NGC 2935	$-0.0034 \pm 0.0003$	$0.0019 \pm 0.0004$	–	$8.649 \pm 0.02$	$8.714 \pm 0.007$	125.06	
NGC 3081 <sup>†</sup>	$-0.0023 \pm 0.0010$	$0.0142 \pm 0.0009$	$0.024 \pm 0.012$	$8.369 \pm 0.02$	$8.332 \pm 0.009$	75.36	
	$-0.0025 \pm 0.0021$	$0.0187 \pm 0.0018$			$8.22 \pm 0.04$		7.5
NGC 4643 <sup>†</sup>	$0.004 \pm 0.003$	$-0.003 \pm 0.002$	–	$8.751 \pm 0.06$	$8.756 \pm 0.019$	67.16	13.2
NGC 5101 <sup>†</sup>	$-0.028 \pm 0.008$	$-0.004 \pm 0.008$	–	$8.784 \pm 0.03$	$8.780 \pm 0.019$	176.66	3.5

**Notes.** Units are dex/arcsec. <sup>(1)</sup> Central oxygen abundance of gas, estimated with an aperture of 1.2 arcsec, and calculated with the *O3N2* method. <sup>(2)</sup> Central oxygen abundance of gas, as a result of the fit, calculated with the *O3N2* method. <sup>(3)</sup>  $R_{25}$  is from the Hyperleda galaxy catalogue. <sup>(5)</sup> AGN-affected region, in arcsec, obtained from Fig. 7. <sup>(†)</sup> Same as Table 4.

**Table 6.** Metallicity gradients in the bulge regions with all the adopted methods for run2 galaxies, including AGN-affected regions.

Galaxy	grad- $R_{23}(M91)$ dex/arcsec	$12 + \log(\text{O}/\text{H})^1$ dex	grad- <i>O2Ne3</i> dex/arcsec	grad- $R_{23}(Z94)$ dex/arcsec	grad- <i>KD03</i> dex/arcsec	grad- <i>P05</i> dex/arcsec	order <sup>2</sup>
NGC 1169	$0.080 \pm 0.007$	$8.47 \pm 0.01$	–	$0.108 \pm 0.015$	$0.086 \pm 0.012$	$0.055 \pm 0.013$	1
NGC 1358 <sup>†</sup>	$-0.08 \pm 0.02$	$8.88 \pm 0.05$	$0.05 \pm 0.04$	$0.16 \pm 0.03$	$-0.069 \pm 0.019$	$-0.15 \pm 0.10$	2
NGC 1530	$0.008 \pm 0.006$	$9.03 \pm 0.02$	–	$0.016 \pm 0.013$	$0.015 \pm 0.009$	$0.023 \pm 0.006$	3
NGC 1832	$-0.038 \pm 0.003$	$9.113 \pm 0.007$	–	$-0.053 \pm 0.005$	$-0.020 \pm 0.003$	$-0.053 \pm 0.004$	4
NGC 2273 <sup>†</sup>	$-0.095 \pm 0.007$	$8.892 \pm 0.014$	$-0.01 \pm 0.02$	$-0.117 \pm 0.012$	$-0.078 \pm 0.007$	$-0.08 \pm 0.01$	5
NGC 2523	$0.054 \pm 0.010$	$8.58 \pm 0.02$	–	$0.082 \pm 0.017$	$0.058 \pm 0.011$	$0.053 \pm 0.014$	6
NGC 2681 <sup>†</sup>	$-0.011 \pm 0.003$	$8.987 \pm 0.007$	–	$-0.005 \pm 0.005$	$-0.011 \pm 0.001$	$-0.018 \pm 0.004$	7
NGC 2859 <sup>†</sup>	$0.037 \pm 0.003$	$8.762 \pm 0.009$	–	$0.046 \pm 0.006$	$0.024 \pm 0.003$	$0.036 \pm 0.006$	8
NGC 2962	$0.109 \pm 0.006$	$8.48 \pm 0.01$	–	$0.111 \pm 0.012$	$0.104 \pm 0.009$	$0.178 \pm 0.010$	9
NGC 4314 <sup>†</sup>	$0.0189 \pm 0.0012$	$8.871 \pm 0.005$	$-0.11 \pm 0.16$	$0.034 \pm 0.002$	$0.0192 \pm 0.0015$	$0.0106 \pm 0.0019$	10
NGC 4394 <sup>†</sup>	$0.035 \pm 0.010$	$8.671 \pm 0.017$	–	$0.044 \pm 0.017$	$0.042 \pm 0.011$	$0.053 \pm 0.015$	11

**Notes.** <sup>(1)</sup> Central oxygen abundance in the gas, as a result of the fit in the bulge region, calculated with the  $R_{23}$  (M91) method. <sup>(2)</sup> See Figs. 12 and 13. <sup>(†)</sup> Same as Table 4.

**Table 7.** Metallicity gradients in the bulge regions, with all the used methods, for run1 galaxies, including AGN regions.

Galaxy	Grad- <i>N2</i> dex/arcsec	$12 + \log(\text{O}/\text{H})^1$ dex	Grad- <i>O3N2</i> dex/arcsec	Grad- <i>SBI</i> dex/arcsec	Order <sup>2</sup>
NGC 1433 <sup>†</sup>	$-0.001 \pm 0.006$	$8.665 \pm 0.017$	$0.024 \pm 0.006$	$0.01 \pm 0.01$	12
NGC 2217 <sup>†</sup>	$-0.045 \pm 0.006$	$8.698 \pm 0.018$	$0.003 \pm 0.005$	$-0.023 \pm 0.012$	13
NGC 2665	$0.008 \pm 0.007$	$8.709 \pm 0.018$	$0.012 \pm 0.006$		14
NGC 2935	$0.005 \pm 0.004$	$8.653 \pm 0.016$	$0.015 \pm 0.004$		15
NGC 3081 <sup>†</sup>	$0.002 \pm 0.005$	$8.376 \pm 0.015$	$-0.003 \pm 0.005$	$0.022 \pm 0.015$	16
NGC 4643 <sup>†</sup>	$0.009 \pm 0.004$	$8.73 \pm 0.02$	$0.004 \pm 0.004$		17
NGC 5101 <sup>†</sup>	$-0.028 \pm 0.008$	$8.780 \pm 0.019$	$-0.004 \pm 0.008$		18

**Notes.** <sup>(1)</sup> Central oxygen abundance in the gas, as a result of the fit in the bulge region, calculated with the *O3N2* method. <sup>(2)</sup> See Figs. 12 and 13. <sup>(†)</sup> Same as Table 4.

are classified as AGNs. If we consider *SBI*, a nebular metallicity is of the same order as the stellar metallicity for NGC 3081 (Sy) and NGC 2217 (LINER).

For some of the other galaxies, the distribution of the gas and the stellar abundances closely follow each other and for 3 galaxies the gas abundances lie clearly ( $\geq 0.2$  dex) above the stellar metallicities.

Not many works have addressed a direct comparison between the metallicities obtained from the stars and the ionized gas. Storchi-Bergmann et al. (1994) concluded that both

abundance measurements are well-correlated for star-forming galaxies. However, recent work (Marino et al. 2011) suggests, as derived from HI and GALEX UV imaging, the presence of current star formation activity in early-type galaxies with emission lines. This sort of galaxy rejuvenation could be due to external gas re-fueling. This accretion would indicate that there are differences between the metallicities of the old stellar component and the newly accreted gas responsible for the present star formation. Furthermore, Annibali et al. (2010) found in a comparison between nebular and stellar metallicities of E-S0 galaxies

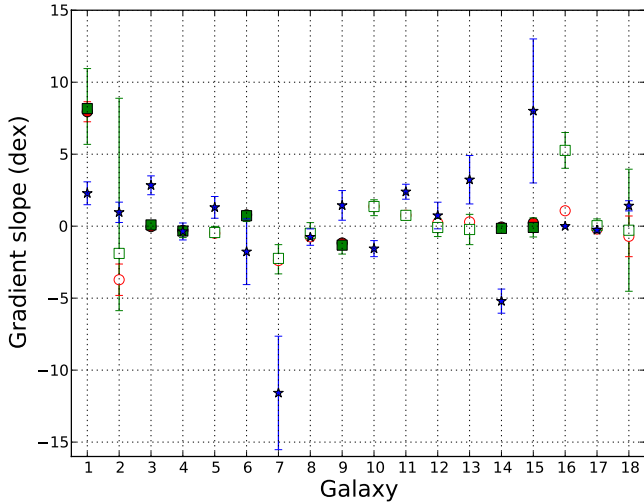


**Fig. 12.** Comparison of the metallicity gradients obtained for the gaseous and stellar components in the bar region of our sample galaxies. They are normalized to  $R_{25}$  (i.e. the gradients have been obtained from linear fits to the  $12 + \log(\text{O}/\text{H})$  versus  $R/R_{25}$  representation for each galaxy). Circles are those estimated with the  $R_{23}$  (M91) or  $N2$  methods, squares are the mean value of gradients calculated with all methods (the error bar covers the range of these gradients), and stars are the gradient  $[\text{Z}/\text{H}]$  for the stellar component (Paper II). Order indicated along the abscissas is that of Tables 6 and 7. Filled symbols represent star-forming galaxies.

with nebular emission that the gas metallicity tends to be lower than the stellar metallicity, the effect largest being for the highest stellar metallicities.

In Figs. 12 and 13, we compare the gradients obtained for the oxygen abundances along bars and the bulge regions with those estimated in Paper II. They are normalized to  $R_{25}$  ( $(12 + \log(\text{O}/\text{H}))/R/R_{25}$ ) values. In Paper I, we found that the stellar metallicity gradients along the bar show a large variety. The distribution of the gas nebular abundances in the bar region have a mild gradient (flatter than for the stellar component for star-forming galaxies except for NGC 1169), and we do not see any clear relation between the stellar and nebular gas metallicity gradients. With respect to the bulge region, gradients for the stellar component in star-forming galaxies are flatter than the gaseous gradients for NGC 1169 and NGC 2523. In the studiable cases, the oxygen abundance gradients are, in general, steeper for bulges than bars, and have the same sign. However, this is not the case for the stellar abundance gradient, where the sign between the bulge and the bar gradient changes in 10 out of 16 galaxies.

## 5. Discussion

We have found that most of the emission is centrally concentrated in the bulge region. This had been noted in previous studies and seems to be independent of the presence of a bar (Davis et al. 2011). In 5 galaxies, emission lines are present along the whole extension of the bar, and 6 out of the 18 galaxies have some star formation at the bar ends as well as in the bulge region. Previous works have claimed that the distribution of star formation in a bar is correlated with the bar age; younger bars ( $< 1$  Gyr) host star formation along the entire bar, while older bars have star formation at the bar-ends and nuclear regions (Phillips 1993; Martin & Friedli 1997; Martin & Roy 1995; Friedli & Benz 1995; Verley et al. 2007). However, some of the galaxies for

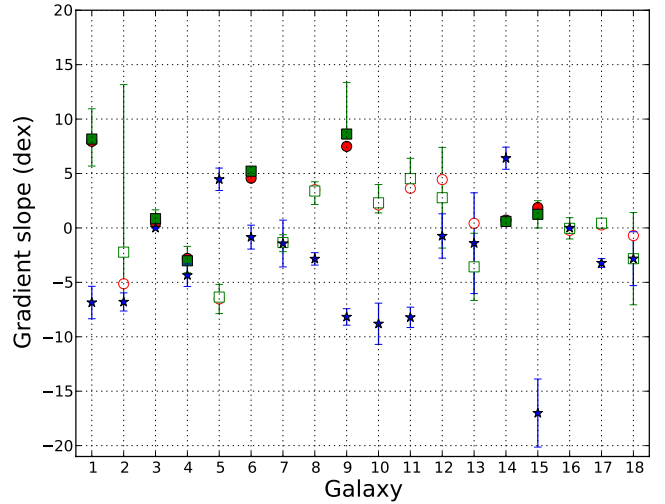


**Fig. 13.** Comparison between metallicity gradients obtained for gaseous and stellar components in the bulge region of our sample galaxies. They are normalized to  $R_{25}$  (i.e. the gradients have been obtained from linear fits to the  $12 + \log(\text{O}/\text{H})$  versus  $R/R_{25}$  representation for each galaxy). Circles are those estimated with the  $R_{23}$  (M91) or  $N2$  methods, squares are the mean value of gradients calculated with all methods (the error bar covers the range of these gradients), and stars are the gradient  $[\text{Z}/\text{H}]$  for the stellar component (Paper II). The order along the abscissas is that of Tables 6 and 7. Filled symbols represent star-forming galaxies.

which nebular gas is found along the bar seem to host bars that are old (see Paper I). Therefore, the star formation distribution in these bars is possibly more related to the reservoirs of gas that could replenish the bar than to the actual time of bar formation.

We have found neither a relation between the difference in abundance values between different methods and the type of the galaxy, nor any relation to the galactocentric distance in which the lines are measured (see Sects. 4.2.1 and 4.2.2).

We have considered the possible systematic effect of an AGN nuclei on the determination of abundances. Its effect is difficult to quantify, but very important when comparing with the stellar metallicities in the inner regions of these galaxies and deriving the abundance gradients. The central regions consist of a mixture of different components with different physical properties (Lindblad & Fathi 2011) and introduce difficulties in determining the main ionising mechanisms. Most of the central abundances derived in the works mentioned above, have not considered the influence of an active nuclei. Their abundance estimations have been carried out in  $\text{H II}$  regions or/and in star-forming galaxies, so the models for calibration are based on stellar photoionization alone. Storchi-Bergmann et al. (1998) proposed two calibrations for active galaxies: the first one depending on  $[\text{N II}]/\text{H}\alpha$  and  $[\text{O III}]/\text{H}\beta$  (SB1), and the second, a linear combination of  $\log [\text{N II}]/\text{H}\alpha$  and  $[\text{O II}]/[\text{O III}]$  (SB2). They concluded that, when possible, the best option is to use the mean value of both. Based on the extrapolation of metallicities towards the nuclear regions, they found that this calibration is good for Seyferts, but that there is no clear conclusion for LINERs. We have used this method, SB1, for only three galaxies of run1. We have been unable to estimate SB2 for them because we could not measure  $[\text{O II}]$ . For these galaxies, 2 LINERs and a Sy, we have compared abundances calculated with SB1 and  $N2$  and  $O3N2$ , which would be the extreme cases i.e. of either AGN or photoionization produced by hot stars. For LINERs, the results of SB1 match or are closer to those of  $O3N2$  in the

central regions, while for the Seyfert galaxy they are similar to those estimated with  $N2$ . In any case, the difference between oxygen abundances derived using  $N2$  or  $SBI$  is less than 0.2 dex, a value considered as the intrinsic uncertainty in the models used to calibrate  $R_{23}$ . Although the presence of an AGN does not seem to alter the results, we caution that the results for these regions may be influenced by AGNs.

We then compared the oxygen abundances with the stellar metallicities. We found that the central metallicities,  $12 + \log(O/H)$ , have a mean value within 1.2 arcsec in the range from 8.4 to 9.1. These values agreed with those found in the inner parts of early-type spirals. Oey & Kennicutt (1993) studied H II regions in 15 Sa to Sb galaxies, obtaining abundance values, derived using the  $R_{23}$  method, from 8.7 to 9.2. The larger values correspond to regions located at smaller galactocentric radii. They found that gas metallicities in these galaxies are systematically higher than those in Sc and later-type galaxies. Zaritsky et al. (1994) suggested that this relation might be indicative of a dependence on galaxy mass and not with galaxy type after analyzing H II regions in a sample of 39 galaxies covering morphological types from Sab to Sd. They found metallicities in the range 8.2–8.6, similar to the abundances of our work, although we cover morphological types from SB0 to SBbc. Vila-Costas & Edmunds (1992) also found a correlation between the central gas abundances and galaxy masses, by analyzing the gas metallicity distribution of 32 disk galaxies of different morphological types. For the centers of Sab-Sb galaxies they found oxygen abundances in the range 8.7–9.5. A large statistical study using SDSS data by Tremonti et al. (2004) analyzed 53 000 star-forming galaxies at  $z \sim 0.1$ . In this study, the authors addressed the fundamental role that the galaxy mass plays in its chemical evolution. They found a strong correlation between mass and nebular oxygen abundance for galaxies with masses between  $10^{8.5}$  and  $10^{10.5} M_{\odot}$ , with a flattening of the relation for higher galaxy masses. Some recent studies investigating how mergers and bars can modify this correlation (Ellison et al. 2011) have measured a higher nebular abundance in barred than unbarred galaxies of the same mass. Our galaxies lie on the flat part of the correlation, hence we do not expect to find any strong correlation between the rotational velocity and the nebular abundance.

However, we see in Fig. 14 that the galaxies with the lowest abundances are those with the highest rotational velocities, although there is a large dispersion in the values, since we also find galaxies with high rotational velocity and high ionized gas metallicities. However, there are no galaxies with low ( $12 + \log(O/H) < 8.68$ ) nebular abundances and low rotational velocities. The only exception is NGC 3081 (Seyfert) for the oxygen abundance obtained using  $O3N2$ . This result might indicate that we cannot exclude the idea that some rejuvenation mechanism operates in some of the most massive galaxies in our sample.

Following this result for the trend in nebular abundances with disk rotational velocities, we search for nebular abundance trends with stellar velocity dispersion, but we find no such trend. As for the stellar abundances, we find in Paper II, as expected from other studies, a correlation between stellar central abundances and central velocity dispersion (see Fig. 15).

When comparing these central nebular abundances with central stellar metallicities, we find that for three galaxies the nebular abundances are significantly lower than the stellar metallicities. The galaxies which show nebular abundances lower than the stellar metallicities are systematically among the galaxies with the highest rotational velocities in our sample.

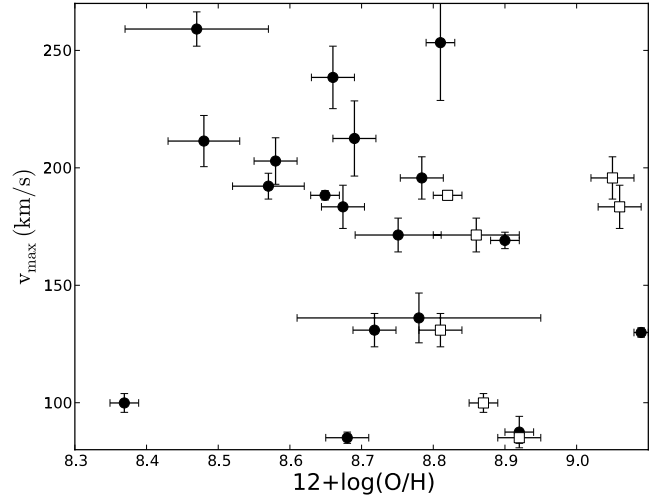


**Fig. 14.** Rotational velocity corrected for inclination versus central oxygen abundances (1.2 arcsec). Filled circles represent those calculated using the  $R_{23}$  method for run2 and  $O3N2$  for run1. Squares are values obtained with  $N2$  for run1.

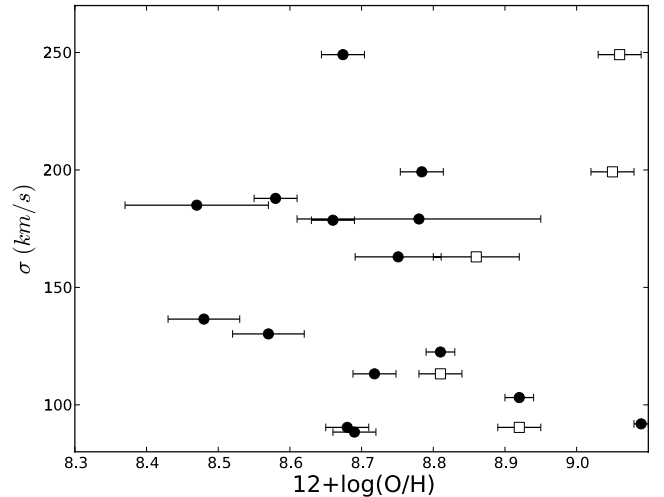


**Fig. 15.** Stellar velocity dispersion versus central oxygen abundances (1.2 arcsec). Filled circles represent those calculated using the  $R_{23}$  method for run2 and  $O3N2$  for run1. Squares are values obtained with  $N2$  for run1.

The bar is thought to provide an efficient mechanism for quickly redistributing material within the disk. External accretion via the bar potential is a plausible mechanism for bringing new gas to the center and diluting the central gas metallicities. The strength of the bar determines the gas inflow rate (e.g. Athanassoula 1992, 2000), although no clear trend between the bar strength and nebular composition is found for our galaxies. The efficiency of this process might be limited by the availability of gas, and despite no clear trend with HI mass being found we note that we lack information about the total gas content of our galaxies. Other processes capable of explaining the existence of low metallicity gas at the center of these massive galaxies include cold flows to the center (Kereš et al. 2005) and particular star-formation histories (Yates et al. 2012). Yates et al. (2012) conclude, by examining semi-analytical models, that massive galaxies with low nebular abundances have undergone a gas-rich merger with a later shut-down of star formation. This low density metal-poor gas accretion is insufficient

to form stars efficiently and subsequently dilutes the gas-phase metallicities. Further information of the total gas content and both its distribution and kinematics would help us to elucidate the different external accretion mechanisms that might operate in these galaxies.

As for the nebular abundance gradients found in this work, numerical models of barred galaxies (Friedli et al. 1994) show that the initial slope of the abundance is only slightly modified in the bar region, while outside the bar corotation radius, the original slope gets flatter. We estimated the gas oxygen abundances along the bars to study the efficiency of mixing by the bar within the corotation radius. Considering only star-forming galaxies, we find positive gradients, with a  $3\text{-}\sigma$  significance, for the oxygen abundance in the bar regions of three galaxies and negative gradients in two other galaxies. The estimated gradient values range from  $-3.7$  to  $1.4$ , in units of  $\text{dex}/(R/R_{25})$  with the aforementioned exception of NGC 1169. In eight of the observed galaxies, the gradient is shallower than  $0.5 \text{ dex}/(R/R_{25})$ . In the bulge region, where most of the emission is found, we find steeper gradients.

It is, however, not a simple task to interpret the origin of these gradients because it is not only stellar evolution, star formation, and bar dynamics, all complicated processes, that affect the gradients but the refueling of newly accreted gas could also change the gradient. Naively, central accretion of gas would dilute the inner regions generating a positive gradient, while the effects of radially accreted gas may not be sufficiently evident without proper modeling. However, it would be possibly to reduce a pre-existing gradient because of the rapid mixing and re-activation of star formation in the bar region (Friedli et al. 1994; Friedli & Benz 1995).

Most gas metallicity gradients that can be found in the literature include the whole disk; van Zee et al. (1998) found gradients in the range  $[-0.30, -1.52] \text{ dex}/R_{25}$  for spiral galaxies, and Rupke et al. (2010) a mean value of  $-0.57 \pm 0.05$  considering 11 isolated spirals. Oey & Kennicutt (1993) concluded that barred galaxies have a shallower gradient than unbarred ones. However, a large range of abundance gradients have been found, some of them being much steeper than for unbarred spirals (Edmunds & Roy 1993; Considere et al. 2000). Vila-Costas & Edmunds found gradients ranging from  $-3.33$  to  $-0.899$  for non-barred galaxies, and from  $-0.156$  to  $-0.398$  for barred galaxies (all in  $\text{dex}/R_{25}$ ). Zaritsky et al. (1994) obtained a mean value of  $-0.23 \text{ dex}/R_{25}$  for five barred galaxies. In particular, for the Milky Way, Balsa et al. (2011) measured a radial gradient of  $-0.0446 \pm 0.0049 \text{ dex}/\text{kpc}$ . Edvardsson (2002) found a value of  $-0.07 \pm 0.01 \text{ dex}/\text{kpc}$  for galactocentric distances of between 6 and 18 kpc.

The discrepancy between the values found in the literature for the disk and our values, concerning only the bar region, could be due to the predicted change in the slope around the bar radius (Friedli et al. 1994). Furthermore, we have found a slope change between the bulge and the bar region, which was also predicted by Friedli et al. (1994). These changes in the abundance slope with radius, such that the gradient is steeper in the inner parts of the galaxies, have been analyzed by various authors. Zaritsky et al. (1994) found that the gradient in the bar of NGC 3319 was different from that outside it. This question was studied by later works, trying to detect a radial variation in the gradient. For instance, for the barred galaxy NGC 3359, Martin & Roy (1995) found a radial variation in the gradient that was, in turn, studied by Zahid & Bresolin (2011), who estimated a break at a characteristic radius. Balsa et al. (2011) concluded that there were no radial discontinuities in the oxygen abundance gradient

for the Milky Way, but that the gradient varies with the azimuth between  $-0.03$  and  $-0.07 \text{ dex}/\text{kpc}$ .

Previous works have assessed the effects of AGNs on the nebular abundance gradients. Annibali et al. (2010) showed that the nebular abundances, increase with radius when derived with the  $R_{23}$  method, but decrease when using methods that take into account harder ionising sources (i.e. AGN), such as the SB method, which is a combination of SB1 and SB2. We have checked whether our gradient calculation could be biased in the same way. We have been able to estimate SB1 for three run1 galaxies, NGC 1433, NGC 2217, and NGC 3081. For them, we did not measure  $[\text{O II}]$ , so cannot calculate  $R_{23}$ , but only  $N2$  and  $O3N2$ . We have found that  $SB1$  gradients are nearly flat for NGC 1433 and NGC 3081, and have the same sign as that derived using  $N2$  for NGC 2217.

Previous studies have attempted to correlate the observed nebular metallicity gradients with the physical properties of the galaxies. Zaritsky et al. (1994) suggested that there is a correlation between the gradient and the bar-type as previously noted by Pagel & Edmunds (1981), Martin (1992), and Edmunds & Roy (1993). We have not found any correlation between the estimated gradients and the physical properties of galaxies, such as bar-type, HI mass, or central stellar velocity dispersion. However, we have analyzed a small range of masses and morphological types. Further studies covering a larger range of galaxy parameters and galactic radii will be necessary to draw stronger conclusions about the correlation between nebular abundance gradients and the physical properties of galaxies.

## 6. Summary and conclusions

We have carried out a detailed analysis of the nebular abundances along the bar and in the bulge of a sample of 20 early-type galaxies to compare them with the stellar abundance distributions obtained in previous works using line-strength indices. We have focused on several relations, in particular: (1) the distribution of abundances and star formation and the properties of the galaxies; (2) the identification of the ionizing mechanisms and the relative influence of the AGN; and (3) the relation between both abundances and rotational velocities and the velocity dispersion in the bulge. We have found that most of the emission in our sample of galaxies is concentrated in the bulge components. We have used several different methods developed for star-forming galaxies to estimate the nebular abundances. Our results on gaseous metallicity gradients and comparison with the stellar metallicities do not depend on the method used. In three galaxies, the estimated nebular abundances lie clearly below the stellar metallicities. Furthermore, we see that the galaxies with the lowest abundances are those with the largest rotational velocities; although there is a large dispersion in the values, this effect might be the result of a central rejuvenation mechanism in the most massive and late-type galaxies. The comparison between the gaseous and stellar metallicities shows that in most galaxies the slope for the nebular abundance distribution in the bulge region is shallower than that of the stellar metallicity. We can conclude that the combination of observations of both gas and stellar metallicities is crucial to determine the star formation histories of galaxies. The study of both phases is very useful to learn about the origin of the gas involved in the star formation; for instance, we clearly see galaxies for which external accreted gas is the fuel source for the present star formation. Owing to the small parameter range covered by our sample, we cannot conclude anything about the role of bars in the mixing, but we observe a variety of gas and stellar metallicity distributions that

indicate that there have been very different mixing and inflow histories from galaxy to galaxy. Therefore, it would be very interesting to complete this study with a wider sample, including later-type and unbarred galaxies.

*Acknowledgements.* We are grateful to the referee for the useful comments and suggestions that have improved the manuscript. We acknowledge the usage of the HyperLeda database (<http://leda.univ-lyon1.fr>). This research has been supported by the Spanish Ministry of Science and Innovation (MICINN) under grants AYA2011-24728, AYA2010-21322-C03-02, AYA2010-21322-C03-03, AYA2007-67625-C02-02 and Consolider-Ingenio CSD2010-00064, and by the Junta de Andalucía (FQM-108). P.S.B. acknowledges support from the Ramon y Cajal Program financed by the Spanish Ministry of Science and Innovation. P.S.B. also acknowledges an ERC grant within the 6th European Community Framework Programme.

## References

- Allende Prieto, C., Lambert, D. L., & Asplund, M. 2001, *ApJ*, 556, L63  
 Alloin, D., Edmunds, M. G., Lindblad, P. O., & Pagel, B. E. J. 1981, *A&A*, 101, 377  
 Annibali, F., Bressan, A., Rampazzo, R., Zeilinger, W. W., & Danese, L. 2007, *A&A*, 463, 455  
 Annibali, F., Bressan, A., Rampazzo, R., et al. 2010, *A&A*, 519, A40  
 Athanassoula, E. 1992, *Physics of Nearby Galaxies: Nature or Nurture?*, Proc. 27th Rencontre de Moriond, eds. T. X. Thuan, C. Balkowski, & J. Tran Thanh Van (Gif-sur-Yvette: Éd. Frontière), 505  
 Athanassoula, E. 2000, *Stars, Gas and Dust in Galaxies: Exploring the Links*, 221, 243  
 Athanassoula, L. 2003, *Galaxies and Chaos*, 626, 313  
 Athey, A. E., & Bregman, J. N. 2009, *ApJ*, 696, 681  
 Baldwin, J. A., Phillips, M. M., & Terlevich, R. 1981, *PASP*, 93, 5  
 Balser, D. S., Rood, R. T., Bania, T. M., & Anderson, L. D. 2011, *BAAS*, 43, #132.03  
 Block, D. L., Puerari, I., Knapen, J. H., et al. 2001, *A&A*, 375, 761  
 Block, D. L., Buta, R., Knapen, J. H., et al. 2004, *AJ*, 128, 183  
 Bresolin, F. 2007, *ApJ*, 656, 186  
 Bresolin, F., Ryan-Weber, E., Kennicutt, R. C., & Goddard, Q. 2009, *ApJ*, 695, 580  
 Buta, R. 1986, *ApJS*, 61, 609  
 Buta, R., Laurikainen, E., Salo, H., Block, D. L., & Knapen, J. H. 2006, *AJ*, 132, 1859  
 Cardiel, N. 1999, Ph.D. Thesis  
 Castellanos, M., Díaz, A. I., & Terlevich, E. 2002, *MNRAS*, 329, 315  
 Chiappini, C., Matteucci, F., & Padoan, P. 2000, *ApJ*, 528, 711  
 Colavitti, E., Matteucci, F., & Murante, G. 2008, *A&A*, 483, 401  
 Considère, S., Coziol, R., Contini, T., & Davoust, E. 2000, *A&A*, 356, 89  
 Davis, T. A., Alatalo, K., Sarzi, M., et al. 2011, *MNRAS*, 1497  
 Denicoló, G., Terlevich, R., & Terlevich, E. 2002, *MNRAS*, 330, 69  
 Dopita, M. A., & Evans, I. N. 1986, *ApJ*, 307, 431  
 Edmunds, M. G., & Pagel, B. E. J. 1984, *MNRAS*, 211, 507  
 Edmunds, M. G., & Roy, J.-R. 1993, *MNRAS*, 261, L17  
 Edvardsson, B. 2002, *Cosmic Chemical Evolution*, 187, 91  
 Ellison, S. L., Nair, P., Patton, D. R., et al. 2011, *MNRAS*, 416, 2182  
 Erwin, P. 2004, *A&A*, 415, 941  
 Filippenko, A. V. 1982, *PASP*, 94, 715  
 Friedli, D. 1999, *The Evolution of Galaxies on Cosmological Timescales*, 187, 88  
 Friedli, D., & Benz, W. 1995, *A&A*, 301, 649  
 Friedli, D., Benz, W., & Kennicutt, R. 1994, *ApJ*, 430, L105  
 Garnett, D. R., & Shields, G. A. 1987, *ApJ*, 317, 82  
 Goddard, Q. E., Bresolin, F., Kennicutt, R. C., Ryan-Weber, E. V., & Rosales-Ortega, F. F. 2011, *MNRAS*, 412, 1246  
 Hidalgo-Gómez, A. M., Ramírez-Fuentes, D., & González, J. J. 2011, *AJ*, in press  
 Howarth, I. D. 1984, *MNRAS*, 203, 301  
 Hummer, D. G., & Storey, P. J. 1987, *MNRAS*, 224, 801  
 Kauffmann, G., Heckman, T. M., Tremonti, C., et al. 2003, *MNRAS*, 346, 1055  
 Jungwiert, B., Combes, F., & Axon, D. J. 1997, *A&AS*, 125, 479  
 Kennicutt, R. C., Keel, W. C., & Blaha, C. A. 1989, *AJ*, 97, 1022  
 Kennicutt, R. C., Bresolin, F., & Garnett, D. R. 2003, *ApJ*, 2009, 748  
 Kereš, D., Katz, N., Weinberg, D. H., & Davé, R. 2005, *MNRAS*, 363, 2  
 Kewley, L. J., & Dopita, M. A. 2002, *ApJS*, 142, 35  
 Kewley, L. J., & Ellison, S. L. 2008, *ApJ*, 681, 1183  
 Kewley, L. J., Dopita, M. A., Sutherland, R. S., Heisler, C. A., & Trevena, J. 2001, *ApJ*, 556, 121  
 Kewley, L. J., Groves, B., Kauffmann, G., & Heckman, T. 2006, *MNRAS*, 372, 961  
 Kobulnicky, H. A., Kennicutt, R. C., Jr., & Pizagno, J. L. 1999, *ApJ*, 514, 544  
 Laurikainen, E., Salo, H., Buta, R., & Vasylyev, S. 2004, *MNRAS*, 355, 1251  
 Lindblad, P.-O., & Fathi, K. 2011, in *Tracing the Ancestry of Galaxies (on the land our ancestors)*, Proc. International Astronomical Union (Cambridge University Press), IAU Symp., 277, 191  
 López-Sánchez, Á. R., & Esteban, C. 2010, *A&A*, 517, A85  
 MacArthur, L. A., González, J. J., & Courteau, S. 2009, *MNRAS*, 395, 28  
 Marino, A., Rampazzo, R., Bianchi, L., et al. 2011, *MNRAS*, 411, 311  
 Márquez, I., Masegosa, J., Moles, M., et al. 2002, *A&A*, 393, 389  
 Martin, P. 1992, Ph.D. Thesis  
 Martin, P., & Friedli, D. 1997, *A&A*, 326, 449  
 Martin, P., & Roy, J.-R. 1995, *ApJ*, 445, 161  
 McCall, M. L., Rybski, P. M., & Shields, G. A. 1985, *ApJSS*, 57, 1  
 McGaugh, S. S. 1991, *ApJ*, 380, 140  
 Moiseev, A. V. 2001, *BSAO*, 51, 140  
 Moustakas, J., Kennicutt, R. C., Jr., Tremonti, C. A., et al. 2010, *ApJS*, 190, 233  
 Nagao, T., Maiolino, R., & Marconi, A. 2006, *A&A*, 459, 85  
 Oey, M. S., & Kennicutt, R. C. Jr. 1993, *ApJ*, 411, 137  
 Osterbrock, D. E. 1989, *Astrophysics of Gaseous Nebulae and Active Galactic Nuclei* (Mill Valley: University Science Books)  
 Pagel, B. E. J., & Edmunds, M. G. 1981, *ARA&A*, 19, 77  
 Pagel, B. E. J., Edmunds, M. G., Blackwell, D. E., Chun, M. S., & Smith, G. 1979, *MNRAS*, 189, 95  
 Pérez, I., & Sánchez-Blázquez, P. 2011, *A&A*, 529, A64 (Paper II)  
 Pérez, I., Sánchez-Blázquez, P., & Zurita, A. 2007, *A&A*, 465, L9  
 Pérez, I., Sánchez-Blázquez, P., & Zurita, A. 2009, *A&A*, 495, 775 (Paper I)  
 Pérez-Montero, E., Hägele, G. F., Contini, T., & Díaz, A. I. 2007, *MNRAS*, 381, 125  
 Pettini, M., & Pagel, B. E. J. 2004, *MNRAS*, 348, L59  
 Pfenninger, D., & Friedli, D. 1991, *A&A*, 252, 75  
 Phillips, A. C. 1993, *BAAS*, 25, 1329  
 Pilyugin, L. S. 2000, *A&A*, 362, 325  
 Pilyugin, L. S. 2001, *A&A*, 369, 594  
 Pilyugin, L. S., & Thuan, T. X. 2005, *ApJ*, 631, 231  
 Portinari, L., & Chiosi, C. 1999, *A&A*, 350, 827  
 Prantzos, N. 2008, *EAS Publ. Ser.*, 32, 311  
 Rola, C. S., Terlevich, E., & Terlevich, R. J. 1997, *MNRAS*, 289, 419  
 Roškar, R., Debattista, V. P., Stinson, G. S., et al. 2008, *Formation and Evolution of Galaxy Disks*, 396, 217  
 Rupke, D. S. N., Kewley, L. J., & Barnes, J. E. 2010, *ApJ*, 710, L156  
 Sánchez-Blázquez, P., Peletier, R. F., Jiménez-Vicente, J., et al. 2006, *MNRAS*, 371, 703  
 Sánchez-Blázquez, P., Gibson, B. K., Kawata, D., Cardiel, N., & Balcells, M. 2009, *MNRAS*, 400, 1264  
 Sanchez-Blazquez, P., Ocvirk, P., Gibson, B. K., Perez, I., & Peletier, R. F. 2011, *MNRAS*, 415, 709  
 Sarzi, M., Rix, H.-W., Shields, J. C., et al. 2005, *ApJ*, 628, 169  
 Seaton, M. J. 1979, *MNRAS*, 187, 73P  
 Schönrich, R., & Binney, J. 2009, *MNRAS*, 399, 1145  
 Storchi-Bergmann, T., Calzetti, D., & Kinney, A. L. 1994, *ApJ*, 429, 572  
 Storchi-Bergmann, T., Schmitt, H. R., Calzetti, D., & Kinney, A. L. 1998, *AJ*, 115, 909  
 Tremonti, C. A., Heckman, T. M., Kauffmann, G., et al. 2004, *ApJ*, 613, 898  
 van Zee, L., Salzer, J. J., Haynes, M. P., O'Donoghue, A. A., & Balonek, T. J. 1998, *AJ*, 116, 2805  
 Vazdekis, A., Sánchez-Blázquez, P., Falcón-Barroso, J., et al. 2010, *MNRAS*, 404, 1639  
 Veilleux, S., & Osterbrock, D. E. 1987, *ApJS*, 63, 295  
 Verley, S., Combes, F., Verdes-Montenegro, L., Bergond, G., & Leon, S. 2007, *A&A*, 474, 43  
 Véron-Cetty, M.-P., & Véron, P. 2006, *A&A*, 455, 773  
 Vila-Costas, M. B., & Edmunds, M. G. 1992, *MNRAS*, 252, 121  
 Wozniak, H., Friedli, D., Martin, P., & Bratschi, P. 1995, *A&AS*, 111, 115  
 Yates, R. M., Kauffmann, G., & Guo, Q. 2012, *MNRAS*, 422, 215  
 Yoachim, P., & Dalcanton, J. J. 2008, *ApJ*, 682, 1004  
 Zahid, H. J., & Bresolin, F. 2011, *AJ*, 141, 192  
 Zaritsky, D., Kennicutt, R. C. Jr., & Huchra, J. P. 1994, *ApJ*, 420, 87

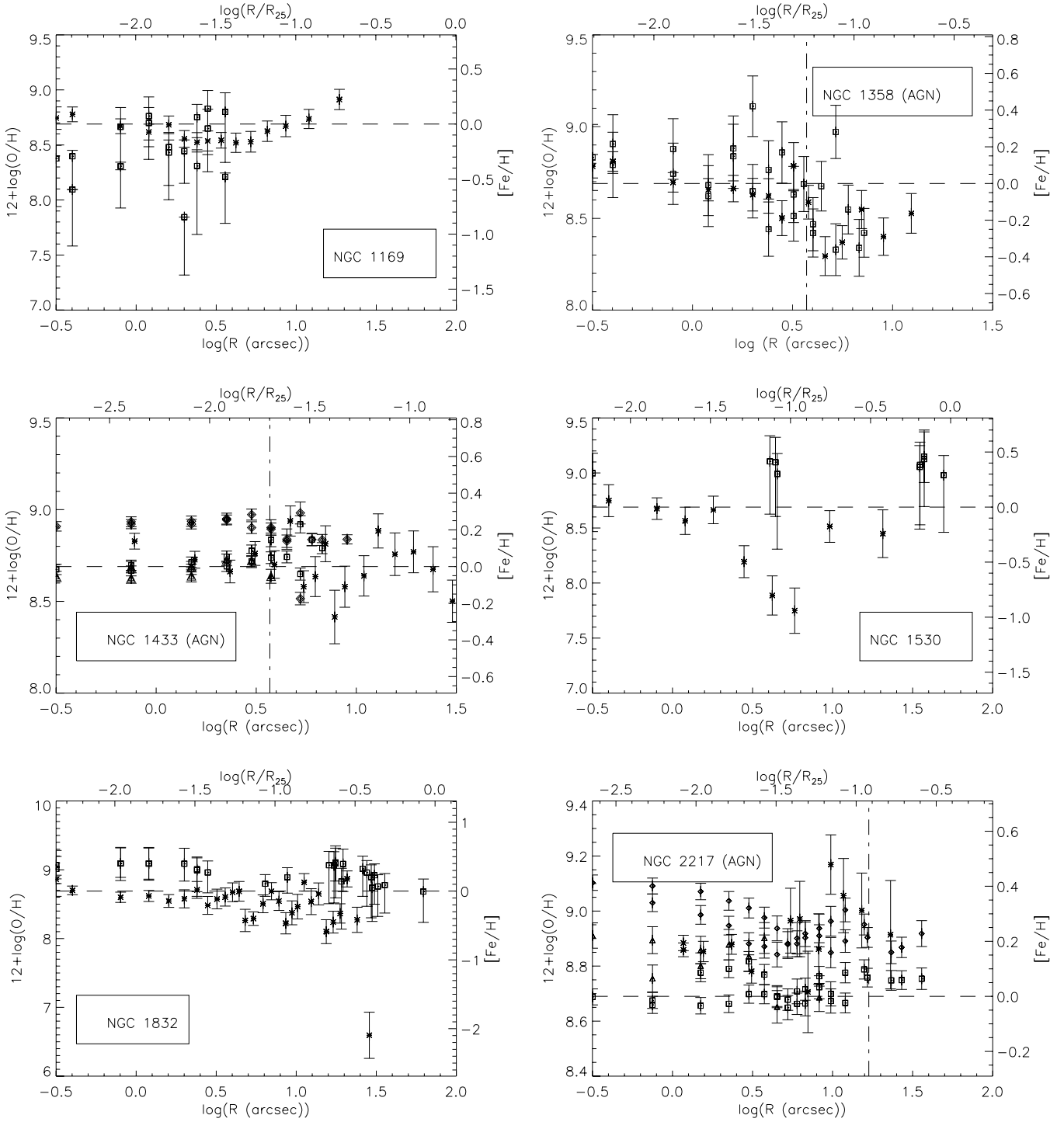


**Fig. 11.** Oxygen gas abundance and stellar metallicities relative to solar as a function of the logarithm of galactocentric radius in arcsec.  $R = 0$  is shifted to  $\log R = -0.5$ . Asterisks indicate metallicities relative to solar obtained from the stellar population (see text for details). Open squares indicate oxygen gas abundances using  $R_{23}$  for run2 galaxies, and error bars cover values obtained with all methods but  $O2Ne3$ . For run1 galaxies, open squares indicate those obtained with  $O3N2$ , diamonds with  $N2$ , and triangles with  $SBI$ . Galaxies hosting AGN are marked, with the vertical lines indicating the region affected by the active nuclei (either as in Fig. 7 or  $3''$ , as indicated in references in Véron-Cetty & Véron (2006)).

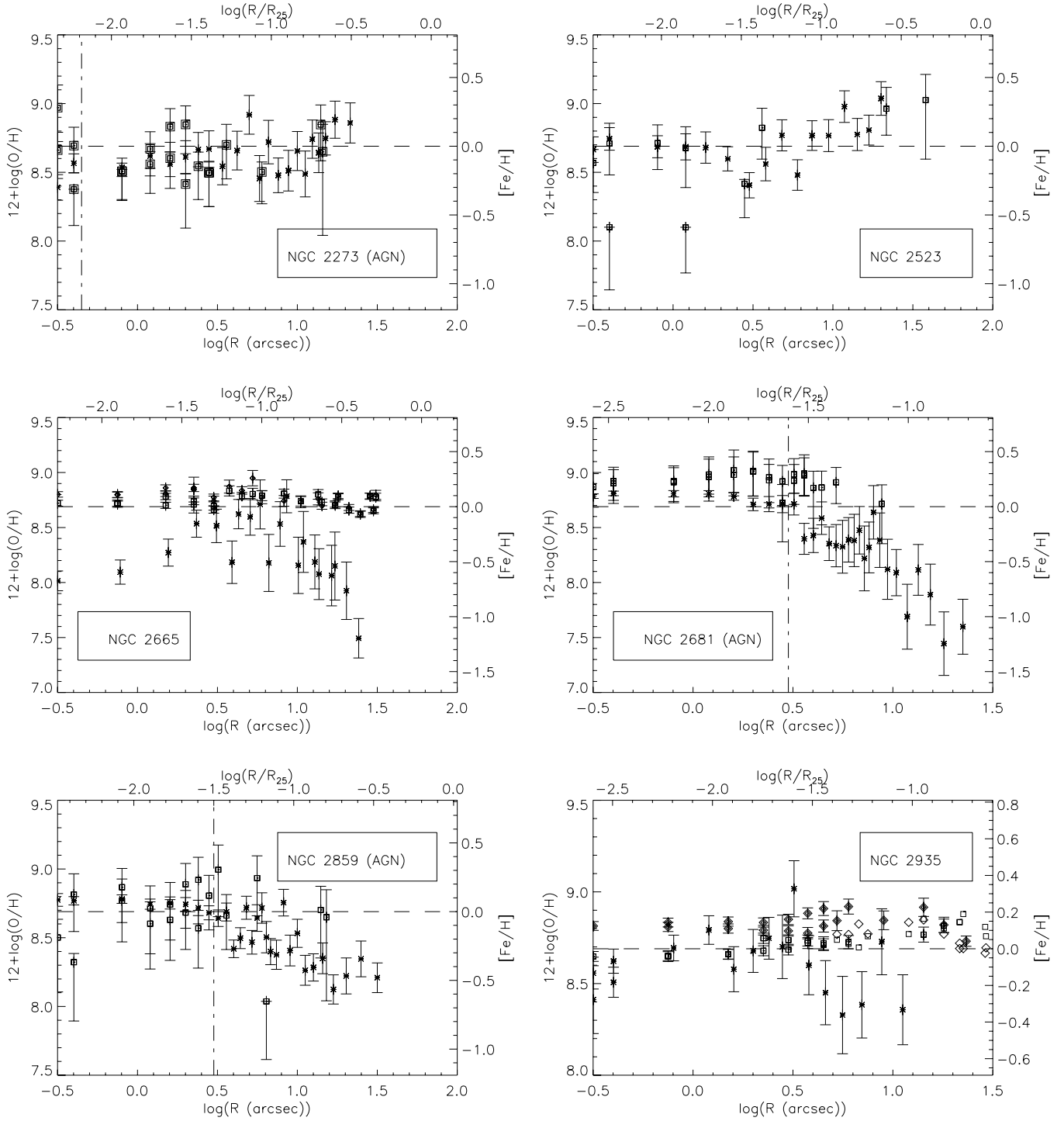


Fig. 11. continued.

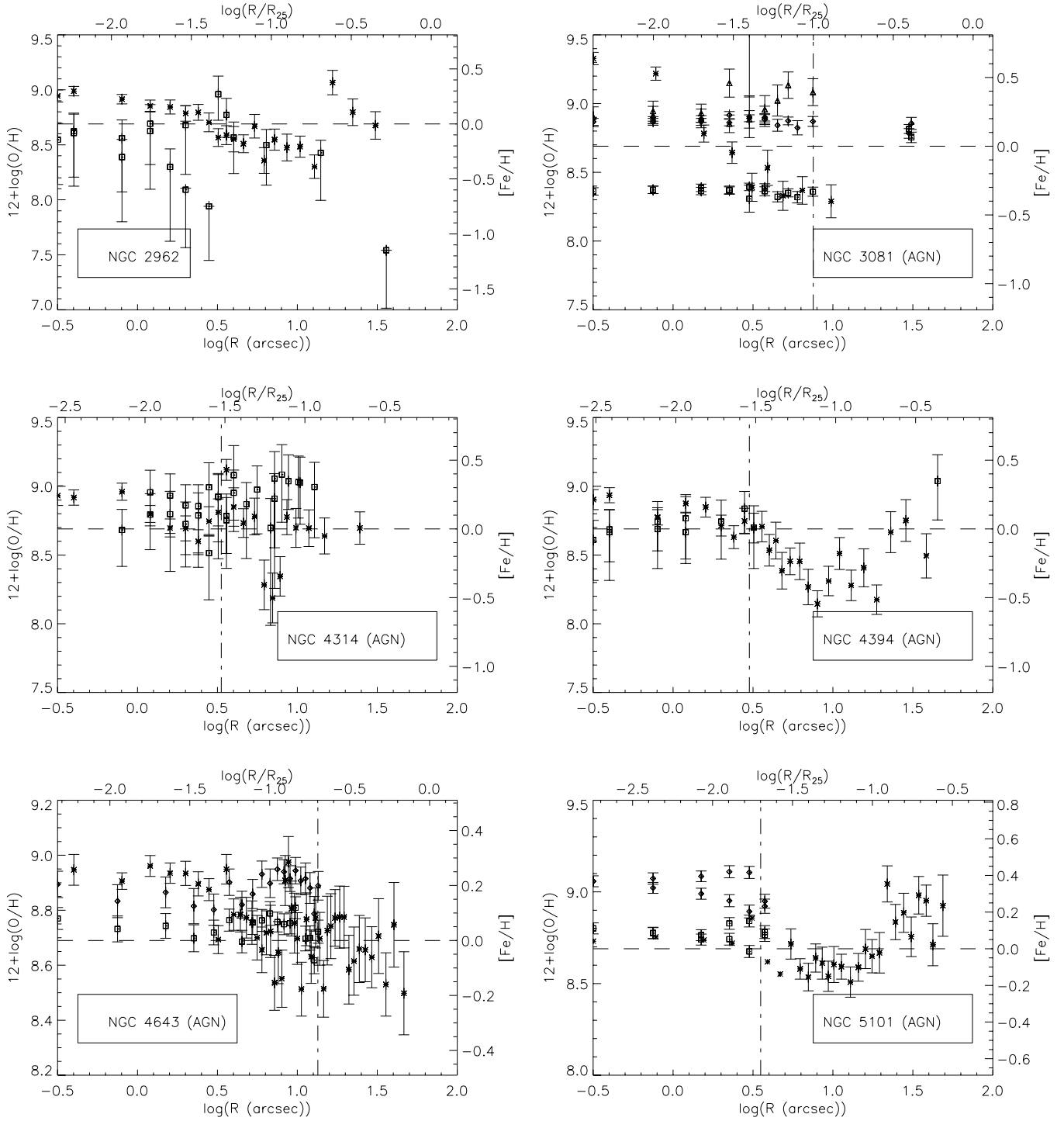


Fig. 11. continued.